



Article

Design and Testing of Innovative Type of Dual-Motor Drive Electric Wheel Loader

Xiaotao Fei ^{1,2}, Yunwu Han ¹, Shaw Voon Wong ^{2,*}, Muhammad Amin Azman ² and Wenlong Shen ^{1,3}

¹ Department of Automobile Engineering, Jiangsu Vocational College of Electronics and Information, Huai'an 223003, China; gs59709@student.upm.edu.my (X.F.); hanyw08@jsei.edu.cn (Y.H.)

² Department of Mechanical & Manufacturing, Faculty of Engineering, Universiti Putra Malaysia, Serdang 43400, Malaysia; amin.azman@upm.edu.my

³ College of Engineering, Nanjing Agricultural University, Nanjing 220031, China

* Correspondence: wongsv@upm.edu.my

Abstract: The electric wheel loader is a new prototype in powertrains and drivetrains that saves energy consumption and diminishes emissions as earthmoving machinery. Dual-motor drive in the front and rear axles of electric wheel loaders helps the distribution of drive torque. However, challenges arise during shoveling conditions, particularly when one motor generates torque exceeding the ground's adhesion force, leading to tire slippage. This study thoroughly examines the mechanical structure of the working unit and elucidates the correlation between wheel load and hydraulic pressure in the base chamber of the tilt cylinder. This analysis is accomplished through a combination of theoretical derivations and experimental tests. The experiments involve a 5 ton rated load electric wheel loader tested across five running cases as well as weighing tests on a 15 ton rated load electric wheel loader. Based on the experiment discoveries, a dual-motor drive electric wheel loader is designed with specific transmission ratios for the front and rear drivetrains, and a torque distribution strategy is proposed based on wheel load during shoveling. Running condition tests demonstrate sufficient drive force for the new electric wheel loader, and shoveling tests reveal a significant reduction in tire slippage when employing the proposed torque distribution strategy compared to evenly distributed torque in the front and rear axles. Moreover, the driving force during the shoveling process remains undiminished. This indicates that the newly designed loader, in conjunction with the proposed strategy, exhibits excellent shoveling efficiency.

Keywords: electric wheel loader; torque distribution; drivetrain; shoveling effect



Citation: Fei, X.; Han, Y.; Wong, S.V.; Azman, M.A.; Shen, W. Design and Testing of Innovative Type of Dual-Motor Drive Electric Wheel Loader. *Energies* **2024**, *17*, 1542. <https://doi.org/10.3390/en17071542>

Academic Editor: Mario Marchesoni

Received: 28 February 2024

Revised: 17 March 2024

Accepted: 22 March 2024

Published: 23 March 2024



Copyright: © 2024 by the authors. Licensee MDPI, Basel, Switzerland. This article is an open access article distributed under the terms and conditions of the Creative Commons Attribution (CC BY) license (<https://creativecommons.org/licenses/by/4.0/>).

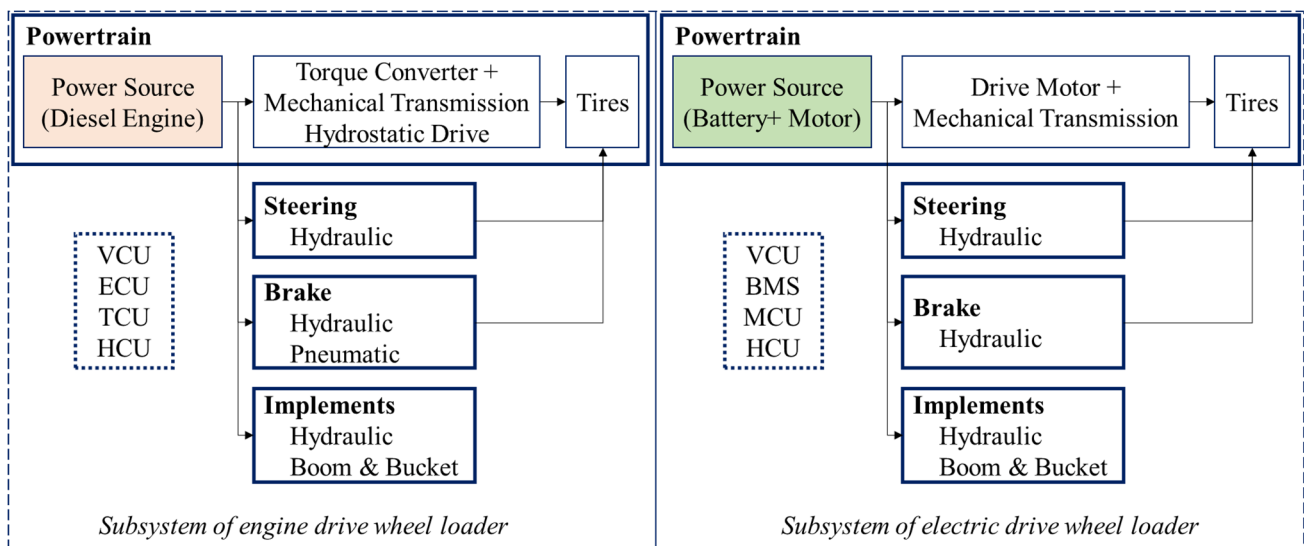
1. Introduction

As an off-road vehicle, the wheel loader (WL) shares numerous similarities in drivetrain and transmission configuration with a four-wheel passenger car. However, the conventional WL is powered by a diesel engine which contributes to large exhaust emission and fuel consumption, as well as working noise. Enhancing fuel efficiency and adopting cleaner energy sources have emerged as pivotal strategies for achieving energy savings and emissions reduction over the past few decades, encompassing various sectors, including the automotive industry [1–4]. The electric wheel loader (EWL) represents a novel category of earthmoving machinery driven by electric motors, playing a crucial role in construction sites, mines, and ports [5]. The statistics from the China Construction Machinery Association (CAMA) reveal that the sales volume of EWLs in China reached 3595 units in the year 2023, with a year-over-year growth of about 210% [6]. Table 1 lists world-famous corporations and their EWL products.

Table 1. Electric wheel loader products across the world.

Country	Company	Model	Bucket Capacity
USA	CAT, Deerfield	950 GC	3.1 m ³
Japan	KUMATSU, Minato	WE2350 (Hybrid)	53 yd ³
China	XCMG, Xuzhou	XC958	2.5–5.0 m ³
Sweden	Volvo, Gothenburg	L25 Electric	1.17 yd ³
China	LiuGong, Liuzhou	862HE	2.7–5.6 m ³

The EWL has become a prominent research topic in recent years [7–10]; researchers need to be aware of structural changes not only in the powertrain but also in the hydraulic system. Figure 1 shows the comparison of engine-drive Ws and electric-drive Ws in subsystems. Other than the power sources that are different, the engine-powered WL typically incorporates a multi-ratio transmission and torque converter, whereas an electric WL is commonly equipped with a fixed-ratio gear reducer, to transmit torque and enlarge it.

**Figure 1.** Comparison of engine-powered and electric wheel loaders in subsystems.

Since the powertrain is no longer diesel-powered, an electric motor is applied to drive the hydraulic system in EWLs [11]. The hydraulic system provides hydraulic energy for the working unit to shovel and dump materials, causing the WL's center of gravity to undergo more frequent changes than that of a passenger car. This results in frequent variations in the drive torque requirements during its operational processes. In a diesel-powered WL, the front and rear axles are interconnected by a transmission shaft, enabling increased drive torque for all four wheels, as a single engine serves as the power source. However, this construction introduces challenges, such as the potential for tire deformation leading to sliding on either the front or rear wheel, owing to varying loads on the axles. Additionally, during shoveling conditions, the forward shift in the gravity center may lift the rear wheels, decreasing vertical pressure and reducing the adhesion force between the rear wheel and the ground either in a conventional engine-drive WL or an electric WL. This scenario can result in wheel slippage under sufficient drive force on the wheels. Both situations contribute to the generation of parasitic power, leading to a substantial consumption of energy. Additionally, the forward shift in the gravity center will cause an increase in vertical load on the front wheels. If the torque distribution on the drive axles is not controlled properly, the energy waste and tire wear will be a big cost for Ws.

Through the discussion and comparison of energy-saving research in Ws, Fei et al. proposed that the control of torque distribution between the front and rear motors of an EWL is essential for achieving energy savings in WL operations [12]. Torque distribution

research on electric vehicles covers topics ranging from two-axle drive [13,14] to four-wheel independent drive [15–17]. In these research fields on EWLs, Yang et al. [18] utilized a group of nonlinear constraint optimization algorithms on the longitudinal dynamics model of EWLs, revealing heightened energy efficiency and improved performance through simulation. Gao et al. [19] employed an unscented Kalman filter to estimate the shoveling load, enabling the calculation of vertical forces on tires. This approach was utilized to distribute drive torque and ultimately reduce tire slippage during shoveling conditions. Wang et al. [20] proposed a torque distribution control strategy grounded in the optimal efficiency of the motor, achieving a 7–12% reduction in energy consumption through simulation when compared to other control strategies. However, in [19], the drive force of wheels was not taken into consideration, which is a vital factor of the shoveling effect. In [18] and [20], they did not test on any EWLs in practical working environments.

Therefore, this study aims to analyze the characteristics of EWLs based on their construction and working processes. The analysis includes examining the relationship between the hydraulic pressure in the base chamber of the tilt cylinder and the force on the bucket. Additionally, this study tests the relationship between the axle load of the front and the hydraulic pressure in the base chamber of the tilt cylinder using a 5 ton rated load EWL and a 15 ton rated load EWL. A new type of dual-motor drive EWL is designed by increasing the transmission ratio of the front drivetrain, and an axle load-based torque control strategy is proposed and tested on the newly designed EWL in running and shoveling conditions.

The contribution of this study is as follows: the linear relationship between the axle load and the hydraulic pressure of the working unit is analyzed and tested. This understanding facilitates the distribution of the drive torque in EWLs without the need for complex algorithms. A distributed drive EWL is designed and manufactured, featuring distinct transmission ratios for the front and rear drivetrains, with the front transmission ratio nearly twice that of the rear. Tests for the new dual-motor drive EWL are conducted under both running and shoveling conditions. The proposed drive torque distribution strategy is applied during the shoveling test, confirming its effectiveness in achieving sufficient drive force and reducing tire slippage when distributing torque according to the axle load.

2. Design Methodology of New EWL

The research methodology's organization is illustrated in Figure 2. Initially, a 5 ton rated EWL is chosen as the test subject. This EWL is propelled by two motors located in the front and rear axles, with identical transmission ratios in both drivetrains. The torque distribution control method is straightforward, evenly distributing torque to both front and rear motors during running and shoveling. Previous research has presented the acquired data and conducted characteristics analyses [21,22].

Building upon insights from the earlier study, the aim is to design a new type of EWL driven by two motors with differing transmission ratios in the drivetrains. This new EWL necessitates a modified control strategy for the distribution of drive torque. The distribution methods include even distribution to the front and rear wheels or distribution based on wheel load, exhibiting a linear relationship with hydraulic pressure in the bucket cylinder. Upon the development and manufacturing of the new EWL, tests under running and shoveling conditions become imperative to validate the drive force and assess the reduction in wheel slippage.

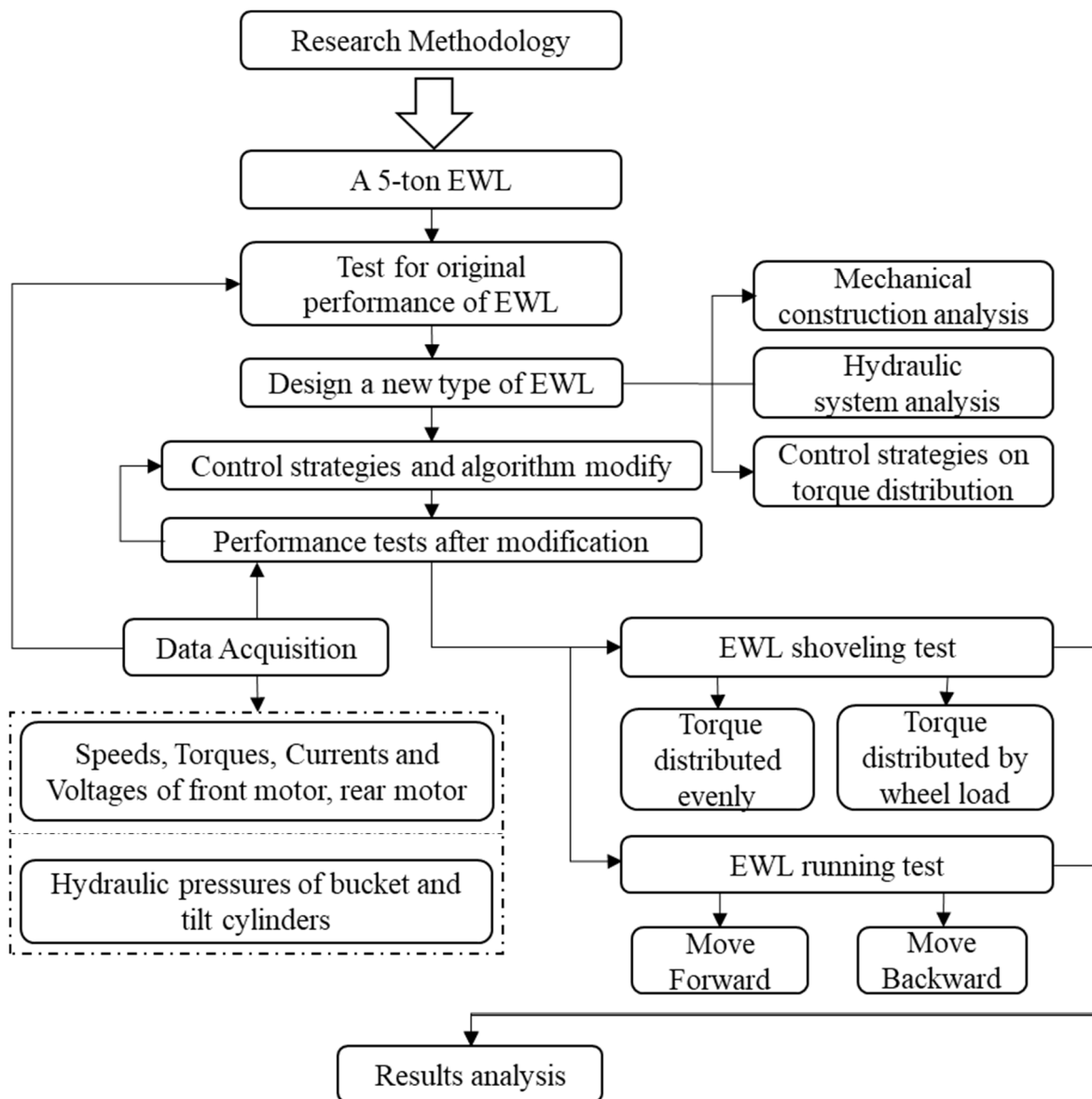


Figure 2. The research flowchart.

2.1. Mechanical Construction Analysis

Figure 3 shows the forces and lever arms of a WL's working unit. N_{f1} is the digging reaction force of the boom, N_{f2} is the pulling force of the bucket link, N_{f3} is the passive force of the bucket tilt cylinder, and N_{f4} is the active force of the boom lift cylinder. L_1 is the lever arm of the bucket cutting edge to point A, L_2 is the lever arm of force N_{f2} to point A, L_3 is the lever arm of force N_{f2} to point E, L_4 is the lever arm of force N_{f3} to point E, L_5 is the lever arm of force N_{f3} to point O, L_6 is the lever arm of force N_{f4} to point O, and L_7 is the lever arm of force N_{f1} to point N.

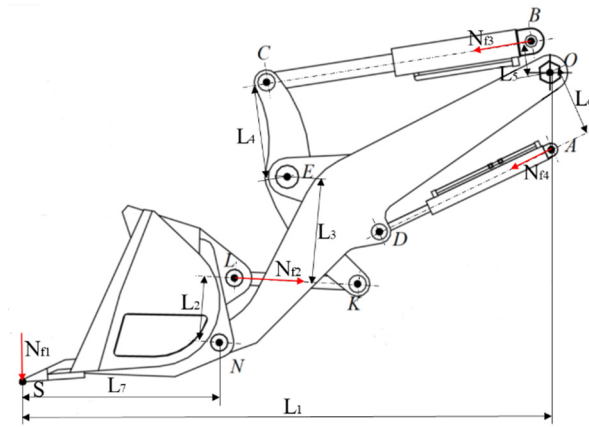


Figure 3. Sketch of working unit's linkage mechanism.

Take the bucket as an isolation body to analyze and calculate the torque at point N . The moment balance at point N can be expressed by Equations (1) and (2).

$$\sum M_N = 0 \quad (1)$$

$$N_{f2} = \frac{N_{f1} \cdot L_7}{L_2} \quad (2)$$

Take the bellcrank CK as an isolation body to analyze and calculate the torque at point E . The moment balance at point E can be expressed by Equations (3) and (4).

$$\sum M_E = 0 \quad (3)$$

$$N_{f3} = \frac{N_{f2} \cdot L_3}{L_4} = \frac{N_{f1} \cdot L_7 \cdot L_3}{L_2 \cdot L_4} \quad (4)$$

Take the working unit as an isolation body to analyze and calculate the torque at point O . The moment balance at point O can be expressed by Equations (5) and (6).

$$\sum M_O = 0 \quad (5)$$

$$N_{f4} \cdot L_6 = N_{f1} \cdot L_1 - N_{f3} \cdot L_5 \quad (6)$$

Equation (7) can be derived from Equations (2)–(4).

$$N_{f1} = \frac{L_2 \cdot L_4 \cdot L_6}{L_1 \cdot L_2 \cdot L_4 - L_3 \cdot L_5 \cdot L_7} \cdot N_{f4} \quad (7)$$

$$N_{f3} = \frac{L_3 \cdot L_6 \cdot L_7}{L_1 \cdot L_2 \cdot L_4 - L_3 \cdot L_5 \cdot L_7} \cdot N_{f4} \quad (8)$$

where N_{f4} is the total force generated by the two boom lift cylinders of the wheel loader.

The value of N_{f4} is equal to the product of the working pressure of the hydraulic system and the area of the base chamber of the boom lift cylinder. The hydraulic pressure is produced by the oil pump, which is powered by the oil motor.

Therefore, in the development of a WL, it is imperative to assess whether the geometric dimensions of the aforementioned working unit meet the specified requirements for overcoming the shoveling forces. Additionally, careful consideration should be given to factors such as hydraulic pressure and cylinder parameters. As long as the length of L_1 to L_7 is fixed or measured, the forces on the base chamber of the tilt cylinder and the base chamber of the boom cylinder can be calculated, as they exhibit a linear relationship.

2.2. Hydraulic System

In the process of shoveling and unloading, the movement of the bucket depends on not only the drivetrain but also the hydraulic mechanism assembled on the wheel loader, including the boom lift cylinder, bucket tilt cylinder, and steering cylinder [23,24]. The boom lift cylinder and bucket tilt cylinder are more considered in this research. The working hydraulic system of this EWL consists of two parts; one is the bucket cylinder with its hydraulic piping and control system, and the other is the tilt cylinder with its hydraulic piping and control system.

The hydraulic oil comes from the hydraulic pump, which is driven by an electric motor [10]. When the pressure of the hydraulic oil in the main pipe connected to the base chamber of the bucket cylinder rises to a value that is large enough to push the piston to move to the piston chamber side, the bucket will rotate upwards. In contrast, if the pressure of the hydraulic oil in the main pipe connected to the piston chamber of the bucket cylinder rises to a value that is large enough to move the piston to the side of base chamber, the bucket will rotate downwards. Similarly, when the oil pressure in the base chamber of the boom tilt cylinders is higher than that in the rod chamber, the piston will be pushed to the side of the rod chamber, and the bucket will be lowered. If the hydraulic oil pushes the piston to the side of the base chamber in the boom tilt cylinders, the bucket will be lifted [25].

In this study, the rated voltage of the hydraulic motor controller is 530 V, and the oil pump works at a constant displacement of 100 mL/r. For the boom lift cylinder, the inner diameter of the cylinder is 160 mm, and the diameter of the piston rod is 90 mm, with a moving stroke of 840 mm. For the bucket tilt cylinder, the inner diameter of the cylinder is 180 mm, and the diameter of the piston rod is 100 mm, with a moving stroke of 585 mm.

2.3. Hydraulic Characteristics of Working Unit

2.3.1. Running Condition Hydraulic Test

In previous research [21,22], the authors analyzed the drive characteristics of the EWL and designed a series of experiments of the EWL traveling in five position states of the front wheels of the loader.

The hydraulic pressure of the working unit of the EWL in the rear motor drive mode is calculated and listed in Tables 2–6. Each smooth segment was selected as the research and analysis database collection. The definition of presented symbols are as follows: \bar{T}_{R_Mot} stands for the average torque of the rear motor in the statistical data segment, \bar{P}_{LB} stands for the average hydraulic pressure in the base chamber of the lift cylinder in the statistical data segment, \bar{P}_{LR} stands for the average hydraulic pressure in the rod chamber of the lift cylinder in the statistical data segment, \bar{P}_{TB} stands for the average hydraulic pressure in the base chamber of the tilt cylinder in the statistical data segment, \bar{P}_{TR} stands for the average hydraulic pressure in the rod chamber of the tilt cylinder in the statistical data segment, and \bar{P}_{R_M} stands for the average output power of the rear motor in the statistical data segment.

Table 2. Hydraulic pressure data calculated in R-drive mode in case L1.

EWL State	Data Segment	\bar{T}_{R_Mot} (N·m)	\bar{P}_{LB} (MPa)	\bar{P}_{LR} (MPa)	\bar{P}_{TB} (MPa)	\bar{P}_{TR} (MPa)	\bar{P}_{R_M} (KW)
Forward 1	962–2785	−142.17	2.78	0.44	0.83	0.43	8.93
Forward 2	7680–9215	−151.22	2.78	0.48	0.86	0.51	9.50
Forward 3	13,676–15,032	−152.82	2.78	0.44	0.85	0.47	9.60
Backward 1	4755–6237	146.00	2.73	0.50	0.87	0.55	9.15
Backward 2	10,829–12,360	135.66	2.66	0.47	0.83	0.55	8.55
Backward 3	16,367–17,882	153.94	2.60	0.44	0.80	0.54	9.65

Table 3. Hydraulic pressure data calculated in R-drive mode in case L2.

EWL State	Data Segment	\bar{T}_{R_Mot} (N·m)	\bar{P}_{LB} (MPa)	\bar{P}_{LR} (MPa)	\bar{P}_{TB} (MPa)	\bar{P}_{TR} (MPa)	\bar{P}_{R_M} (KW)
Forward 1	1000–2800	−306.46	1.27	0.38	0.20	1.80	16.99
Forward 2	7100–9000	−300.55	1.24	0.35	0.19	1.79	18.90
Forward 3	13,200–15,000	−310.22	1.24	0.32	0.18	1.75	19.48
Backward 1	4200–6000	277.34	0.70	0.49	0.18	2.10	17.40
Backward 2	10,200–11,900	277.27	0.68	0.46	0.17	2.10	17.39
Backward 3	16,300–18,100	274.79	0.67	0.44	0.17	2.07	17.24

Table 4. Hydraulic pressure data calculated in R-drive mode in case L3.

EWL State	Data Segment	\bar{T}_{R_Mot} (N·m)	\bar{P}_{LB} (MPa)	\bar{P}_{LR} (MPa)	\bar{P}_{TB} (MPa)	\bar{P}_{TR} (MPa)	\bar{P}_{R_M} (KW)
Forward 1	22,500–24,000	−420.42	0.73	0.26	0.16	1.51	26.40
Forward 2	28,400–30,100	−422.09	0.74	0.29	0.16	1.44	26.50
Forward 3	34,400–36,400	−414.35	0.73	0.27	0.15	1.39	26.01
Backward 1	25,300–27,200	356.72	0.09	0.53	0.16	1.63	22.39
Backward 2	31,400–33,400	369.60	0.10	0.55	0.16	1.29	23.18
Backward 3	37,600–39,100	360.60	0.10	0.55	0.15	1.44	22.62

Table 5. Hydraulic pressure data calculated in R-drive mode in case L4.

EWL State	Data Segment	\bar{T}_{R_Mot} (N·m)	\bar{P}_{LB} (MPa)	\bar{P}_{LR} (MPa)	\bar{P}_{TB} (MPa)	\bar{P}_{TR} (MPa)	\bar{P}_{R_M} (KW)
Forward 1	2000–3800	−532.15	−0.04	1.86	0.09	5.04	33.42
Forward 2	7900–9700	−538.17	−0.04	1.78	0.08	5.03	33.82
Forward 3	14,100–16,100	−541.77	−0.04	1.78	0.07	5.01	34.02
Backward 1	5100–6800	516.19	−0.04	4.31	0.08	5.74	32.36
Backward 2	10,900–12,900	495.65	−0.04	4.14	0.07	5.64	31.10
Backward 3	17,400–19,200	493.43	−0.04	4.08	0.06	5.56	30.94

Table 6. Hydraulic pressure data calculated in R-drive mode in case L5.

EWL State	Data Segment	\bar{T}_{R_Mot} (N·m)	\bar{P}_{LB} (MPa)	\bar{P}_{LR} (MPa)	\bar{P}_{TB} (MPa)	\bar{P}_{TR} (MPa)	\bar{P}_{R_M} (KW)
Forward 1	1300–2800	−609.99	−0.03	2.51	1.70	8.28	38.36
Forward 2	8200–9800	−601.06	−0.03	2.52	1.20	7.49	37.78
Forward 3	15,000–16,400	−606.23	−0.03	2.48	0.88	6.96	38.10
Backward 1	4400–6300	614.13	−0.04	6.61	0.84	9.21	38.54
Backward 2	12,000–13,800	637.45	−0.04	6.62	0.56	8.81	39.96
Backward 3	18,300–19,300	565.92	−0.03	6.44	0.43	8.63	35.50

Table 2 shows the average pressure in the base chamber of the lift cylinder is 2.78 MPa in the moving forward state, while the value is 2.66 MPa in the moving backward state. It also shows the average pressure in the rod chamber of the lift cylinder is 0.45 MPa in the moving forward state, while the value is 0.47 MPa in the moving backward state. The mean values of \bar{P}_{TB} are 0.85 MPa in the moving forward state and 0.83 MPa in the moving backward state. The average values of \bar{P}_{TR} are 0.47 MPa in the moving forward state and 0.55 MPa in the moving backward state.

Table 3 shows the average pressure in the base chamber of the lift cylinder is 1.25 MPa in the moving forward state, while the value is 0.68 MPa in the moving backward state. It also shows the average pressure in the rod chamber of the lift cylinder is 0.35 MPa in the moving forward state, while the value is 0.46 MPa in the moving backward state. The mean values of \bar{P}_{TB} are 0.19 MPa in the moving forward state and 0.17 MPa in the moving backward state. The average values of \bar{P}_{TR} are 1.78 MPa in the moving forward state and 2.09 MPa in the moving backward state.

Table 4 shows the average pressure in the base chamber of the lift cylinder is 0.73 MPa in the moving forward state, while the value is 0.10 MPa in the moving backward state. It also shows the average pressure in the rod chamber of the lift cylinder is 0.27 MPa in the moving forward state, while the value is 0.54 MPa in the moving backward state. The mean values of \bar{P}_{TB} are 0.16 MPa in the moving forward state and 0.16 MPa in the moving backward state. The average values of \bar{P}_{TR} are 1.45 MPa in the moving forward state and 1.45 MPa in the moving backward state.

Table 5 shows the average pressure in the base chamber of the lift cylinder is -0.04 MPa in both the moving forward and backward states. It also shows the average pressure in the rod chamber of the lift cylinder is 1.81 MPa in the moving forward state, while the value is 4.18 MPa in the moving backward state. The mean values of \bar{P}_{TB} are 0.08 MPa in the moving forward state and 0.07 MPa in the moving backward state. The average values of \bar{P}_{TR} are 5.03 MPa in the moving forward state and 5.65 MPa in the moving backward state.

Table 6 shows the average pressure in the base chamber of the lift cylinder of the same nature in both the moving forward and backward states, that is, the value is slightly less than zero, indicating that a small amount of vacuum is generated in the cylinder. It shows the average pressure in the rod chamber of the lift cylinder is 2.50 MPa in the moving forward state, while the value is 6.56 MPa in the moving backward state. The mean values of \bar{P}_{TB} are 1.26 MPa with a relatively larger fluctuation in the moving forward state and 0.61 MPa in the moving backward state. The average values of \bar{P}_{TR} are 7.58 MPa in the moving forward state and 8.88 MPa in the moving backward state.

Comparing the data from Tables 2–6, there are two sets of data that have a more pronounced pattern of change with the backward shift of the WL's center of gravity from case L1 to case L5. The sets of data are the average hydraulic pressure in the base chamber of the lift cylinder and in the base chamber of the tilt cylinder. The change rule of \bar{P}_{LB} and \bar{P}_{TB} is the pressure decreases in general as the front wheel is lifted more either in the state of moving forward or of moving backward, as shown in Table 7.

Table 7. A statistic of average values of the working unit pressure in five cases.

State	Mean Value	L1	L2	L3	L4	L5
Move forward	\bar{P}_{LB}	2.78	1.25	0.73	-0.04	-0.03
	\bar{P}_{LR}	0.45	0.35	0.27	1.81	2.5
	\bar{P}_{TB}	0.85	0.19	0.16	0.08	1.26
	\bar{P}_{TR}	0.47	0.47	1.45	5.03	7.58
Move backward	\bar{P}_{LB}	2.66	0.68	0.10	-0.04	-0.04
	\bar{P}_{LR}	0.47	0.46	0.54	4.18	6.56
	\bar{P}_{TB}	0.83	0.17	0.16	0.07	0.61
	\bar{P}_{TR}	0.47	2.09	1.45	5.65	8.88

2.3.2. Weighing Test for Bucket Hydraulic Pressure

To validate the above regularity, another experiment was carried out. A wheel loader with a 15 ton rated load capacity is used as the test subject, to load different weights on the bucket, testing the vertical force of the rear wheel on the ground and the hydraulic pressures in the base chamber of the lift cylinder and in the base chamber of the tilt cylinder. The vertical force of the rear wheel on the ground is weighed by a platform weighbridge, which is presented in Figure 3. The overall mass of the selected WL is 56.2 tons when there is no load on the bucket, with a front wheel load of 25.9 tons and a rear wheel load of 30.3 tons measured in the transport position, as shown in Figure 4.

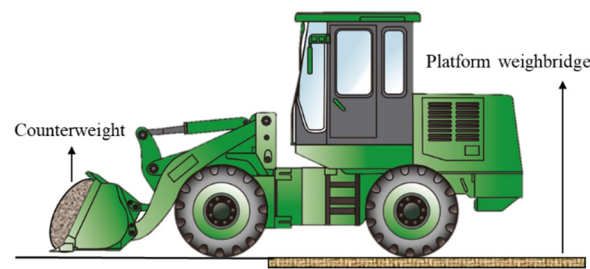


Figure 4. The method to measure the vertical force on the ground of the rear wheel.

The counterweight masses range from zero to 1 ton, 2 tons, 3 tons...one ton at a time, up to 20 tons. The measured data are listed in Table 8. N_B stands for the mass of the counterweight in tons, P_{LB} stands for the hydraulic pressure in the base chamber of the lift cylinder, ΔP_{LB} stands for the change in two adjacent hydraulic pressure measurements in the base chamber of the lift cylinder, P_{TB} stands for the hydraulic pressure in the base chamber of the tilt cylinder, and ΔP_{TB} stands for the change in two adjacent hydraulic pressure measurements in the base chamber of the tilt cylinder. N_R indicates the vertical force on the ground, which is measured by the platform weighbridge, and ΔN_R represents the change of two adjacent N_R measurements.

Table 8. Hydraulic pressure and rear wheel load of WL under different bucket loads.

N_B (t)	P_{LB} (MPa)	ΔP_{LB} (MPa)	P_{TB} (MPa)	ΔP_{TB} (MPa)	N_R (t)	ΔN_R (t)
0	4.9	0.72	2.01	0.48	29.75	0
1	5.62	0.59	2.49	0.3	29.03	0.72
2	6.21	0.6	2.79	0.59	28.33	0.7
3	6.81	0.72	3.38	0.85	27.51	0.82
4	7.53	0.45	4.23	0.27	26.83	0.68
5	7.98	0.98	4.5	1.72	26.05	0.78
6	8.96	0.51	6.22	0.44	24.73	1.32
7	9.47	0.62	6.66	0.45	24.08	0.65
8	10.09	0.32	7.11	0.14	23.22	0.86
9	10.41	0.66	7.25	0.09	22.67	0.55
10	11.07	0.94	7.34	0.64	21.81	0.86
11	12.01	0.65	7.98	0.53	20.53	1.28
12	12.66	0.27	8.51	1.51	19.71	0.82
13	12.93	1.08	10.02	-0.76	18.93	0.78
14	14.01	0.46	9.26	0.54	18.12	0.81
15	14.47	1.45	9.8	0.89	17.33	0.79
16	15.92	-0.29	10.69	1.85	16.44	0.89
17	15.63	0.39	12.54	0.09	15.52	0.92
18	16.02	2.06	12.63	-0.38	14.68	0.84
19	18.08	0.44	12.25	0.47	13.43	1.25
20	18.52	0	12.72	0	13.54	-0.11

Figure 5 shows the relation curve between hydraulic pressure, rear wheel load, and the bucket load based on the data in Table 8. The rule is P_{LB} and P_{TB} increase as the load increases in the bucket, which validates the similar rule as conducted by Table 7. Therefore, the hydraulic pressure in the base chamber of the tilt cylinder can be selected as a reflection of the vertical force of the rear wheel on the ground.

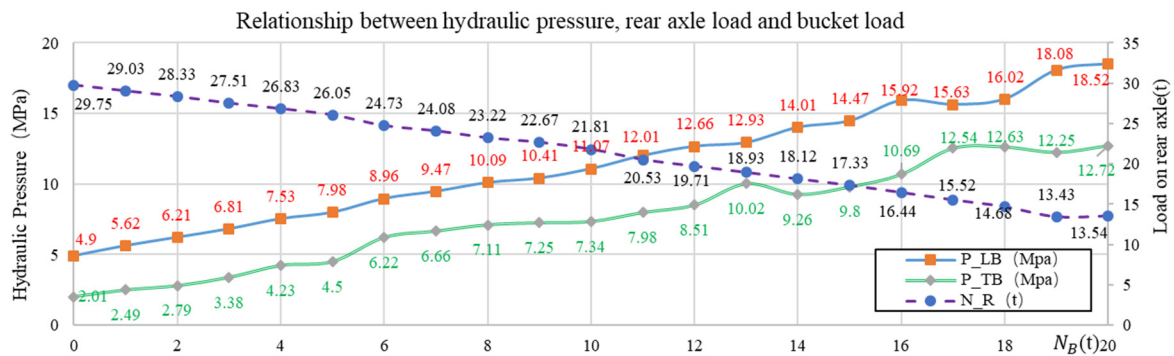


Figure 5. Curve of hydraulic pressure and rear axle load in relation to bucket load.

2.4. Torque Distribution Strategy

Firstly, as an initial step, a trend analysis conducted in Section 2.3 yields a trend table, showcased in Table 9, which outlines alterations in motor torque and energy efficiency as the height of front wheel lifting varies.

Table 9. The alterations in motor torque and efficiency as the front wheel is raised higher [22].

Drive Mode	Torque	Motor Efficiency	State of EWL
F-drive	Increase	Decrease	Forward
	Increase	Decrease	Backward
R-drive	Increase	Decrease	Forward
	Increase	Decrease	Backward
D-drive	Increase	Increase	Forward
	Increase	Increase	Backward

This analysis and the discussion above serve as a foundation for proposing enhancements in motor energy efficiency for dual-motor drive EWLs, offering potential solutions for researchers and manufacturers.

Subsequently, as stated in [22], recommendations are made to optimize motor usage, with a smaller motor designated for the front wheel and a larger one for the rear, supplemented by torque adjustments as needed. During EWL operations, the rear motor can function as the primary drive motor in running conditions, while the front motor can assume this role in shoveling tasks.

Furthermore, tire slippage can be addressed by monitoring the speed of both front and rear wheels and making adjustments to the hydraulic circuit controlling the bucket or boom, thereby restoring traction between the front wheels and the ground.

Last but not least, the structure of the electric drive system can be improved by installing a motor with a smaller rated torque but a reduction gear with a larger transmission ratio on the front axle, while a normal motor and a reduction gear with a smaller transmission ratio are installed on the rear axle. However, a more moderate control algorithm should be applied to this structure.

In the working process of an EWL, the drive torque required T_{Req} is determined by the opening of the accelerator pedal. T_{Req} can be obtained by looking up the Torque-Pedal opening table. When the velocity of an EWL is lower than a fixed value, 10 km/h, for example, the pedal opening is larger than 50%. This may indicate that the resistance is increasing, therefore the overall torque required is increasing. Under these conditions, P_{TB} from the hydraulic pressure sensor can be used as an input parameter, and T_{Req} corresponding to the throttle opening φ_{Acc} can be the target torque, which is generated by the two motors, as expressed by Equation (9).

$$T_{Req} = T_F + T_R \tag{9}$$

To prevent the slippage of the wheels, the following condition in Equations (10) and (11) should be fulfilled without considering mechanical efficiency.

$$T_F = \frac{T_F \cdot i_F}{R_F} < \varphi_F \cdot N_F \tag{10}$$

$$T_R = \frac{T_R \cdot i_R}{R_R} < \varphi_R \cdot N_R \tag{11}$$

where φ_F is the adhesion coefficient of the front wheel, φ_R is the adhesion coefficient of the rear wheel, and N_F indicates the vertical force of the front wheel on the ground.

After meeting the above conditions, the tests for the torque distribution of the front and rear motor can be carried out. The principle of the test is that as the bucket cavity oil pressure P_{TB} increases, the torque will be more allocated to the front drive wheel and less allocated to the rear drive wheel, which is based on the rule conducted in Section 2.3. The test method of torque distribution can be referred to Table 10. P_{TB_MAX} indicates the maximum value of the hydraulic pressure in the base chamber of the tilt cylinder, and P_{TB_MIN} represents the minimum value; both can be measured by the test.

Table 10. Test regularity of torque distribution.

φ_{Acc}	P_{TB}	T_F	T_R
50%	P_{TB_MIN}	$0.5T_{Req}$	$0.5T_{Req}$
51%	$P_{TB_MIN} + \frac{P_{TB_MAX} - P_{TB_MIN}}{50}$	$0.51T_{Req}$	$0.49T_{Req}$
52%	$P_{TB_MIN} + 2 * \frac{P_{TB_MAX} - P_{TB_MIN}}{50}$	$0.52T_{Req}$	$0.48T_{Req}$
.....
99%	$P_{TB_MIN} + 49 * \frac{P_{TB_MAX} - P_{TB_MIN}}{50}$	$0.99T_{Req}$	$0.01T_{Req}$
100%	P_{TB_MAX}	T_{Req}	0

The effectiveness will be judged by recording the data of motor speed, motor torque, and the wheel slippage under different conditions, with the evaluation indicator introduced as Equations (12)–(14).

$$\eta_{F_M} = \frac{9.55T_F \cdot n_F}{U_F \cdot I_F} \times 100\% \tag{12}$$

$$\eta_{R_M} = \frac{9.55T_R \cdot n_R}{U_R \cdot I_R} \times 100\% \tag{13}$$

$$\eta_{D_M} = \frac{9.55 \cdot (T_F \cdot n_F + T_R \cdot n_R)}{U_F \cdot I_F + U_R \cdot I_R} \times 100\% \tag{14}$$

where η_{F_M} is the electricity efficiency of the front motor, η_{R_M} is the electricity efficiency of the rear motor, and η_{D_M} is the overall electricity efficiency of the two motors.

3. Design of New EWL

A new EWL is developed for performance tests and the validation of research objectives. The EWL has a rated load of 5 tons and is mechanically similar to the EWL for the original data acquisition. The overall mass of the EWL is around 18 tons.

3.1. The Power Battery

This EWL is equipped with LiFePO₄ batteries, renowned for their high power density and stability. The battery configuration involves nine cases assembled in a 3S3P arrangement, depicted in Figure 6. Each case consists of 63 cells connected in series and operates at a voltage of 202.86 V. Consequently, the arrangement of the battery package is 3S189P with an output voltage of approximately 615 V, being three times the voltage of an individual case. With each battery case capable of storing 35.09 KWh of electricity, the overall storage capacity of the entire battery package amounts to 315 KWh, reflecting a nine times increase. The detailed parameters of the battery are listed in Table 11.

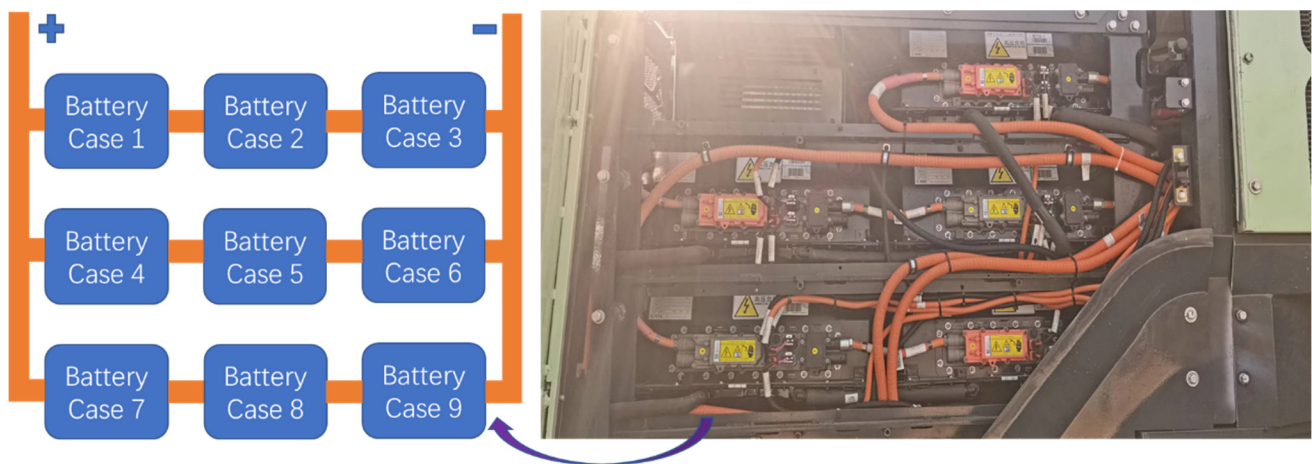


Figure 6. The inner package of the power battery.

Table 11. The technical parameters of the battery.

Items	Parameters	Items	Parameters
Case Type	L173C11	Rated voltage of cell	3.22 V
Case Mass	225 kg	Battery pack form	3P189S
Case Number	9	Rated capacity	519 Ah
Case Voltage	202.86 V	Rated electricity storage	315.85 KWh
Protection level	IP67	Rated voltage	608.58 V

3.2. The Front Drive Axle

Typically, the front drive axle experiences a higher proportion of the driving force compared to the rear axle in shoveling conditions. The torque applied to the wheels is primarily influenced by the motor's output torque and the transmission ratio from the motor to the wheel. The resulting drive force on the ground is additionally influenced by the wheel radius. The diameter of the wheels is 1610 mm. In light of the original EWL's structure and parameters, the new design incorporates a significantly increased transmission ratio of 44.03. This elevated ratio amplifies the motor's output torque nearly 44 times, contributing to an enhanced overall performance.

Figures 7 and 8 depict the 3D graphic and actual photograph, respectively, of the assembled motor of the front drive axle as viewed from the boom. The motor is a commonly used switched reluctance motor (SRM) [26,27], and the parameters are listed in Table 12.

Table 12. The technical parameters of the front motor.

Items	Parameters	Items	Parameters
Motor type	SRM	Model	KTC400-100XZ-SH
Rated torque	1500 N·m	Peak torque	3200 N·m
Rated voltage	618 VDC	Rated power	100 KW
Rated speed	955 rpm	Insulation level	H
Max. speed	3000 r/min	Protection level	IP67
Rated current	170 A	Cooling mode	Liquid
Mass	490 Kg	Efficiency	95%

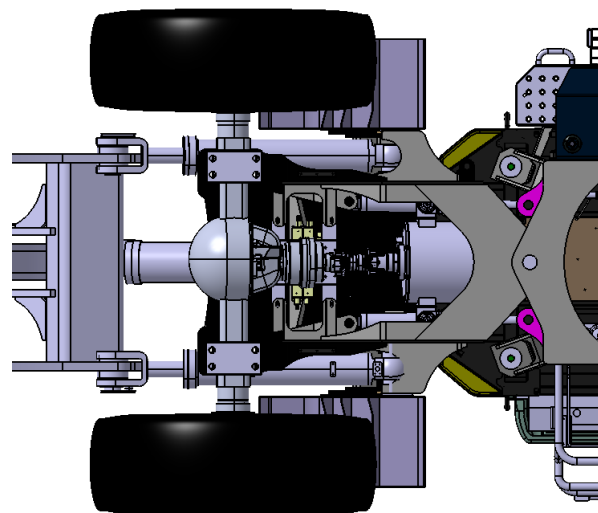


Figure 7. The 3D graphic of the front drive motor.

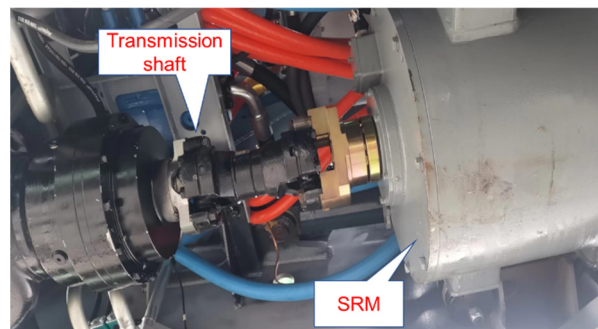


Figure 8. The front drive motor.

3.3. The Rear Drive Axle

As analyzed, the rear drive axle is aimed to drive in running situations. Therefore, the drive force transmitted to the wheels does not need to be that large. The drive force is designed to be no less than the maximum static friction force. The drive motor is a type of PMSM, which is widely applied in construction machinery [28,29], with a rated torque of 1200 Nm, and the parameters are listed in Table 13. The transmission ratio from the motor to the wheel of the rear drive axle is 22.85. Figures 9 and 10 are the 3D and actual pictures of the assembled motor of the rear drive axle.

Table 13. The parameters of the drive motor in the rear axle.

Items	Parameters	Items	Parameters
Motor type	PMSM	Model	DM320H41
Rated torque	1200 N·m	Peak torque	3200 N·m
Rated power	120 KW	Peak power	250 KW
Rated speed	955 rpm	Insulation level	H
Max. speed	3000 rpm	Protection level	IP67
Rated voltage	540 VDC	Cooling mode	Liquid
Mass	240 Kg	Efficiency	95%

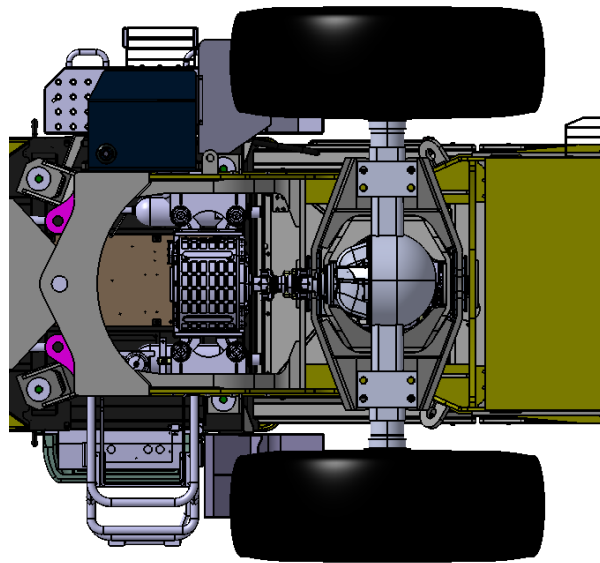


Figure 9. The 3D graphic of the rear drive motor.



Figure 10. The rear drive motor and transfer case.

3.4. The Mechanical Structure of the Working Unit

The working unit mainly consists of a boom and bucket, interconnected by hydraulic cylinders and a mechanical rod, as illustrated in Figure 11. The bucket, constructed from steel with a density of 7850 kg/m^3 , possesses a mass of 2011 kg, constituting 40% of the rated load capacity. Nine chamfered teeth are designed to be installed on the bucket to minimize material resistance, as pictured in Figure 12.

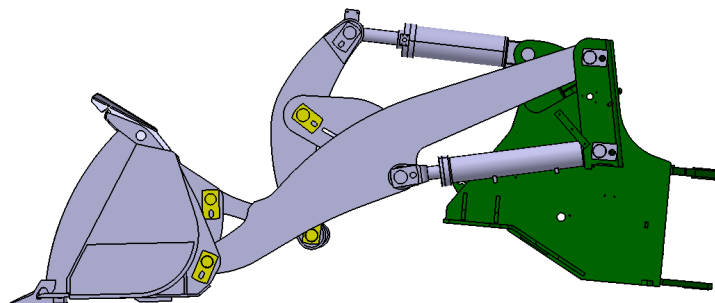


Figure 11. The sketch of the working mechanism.

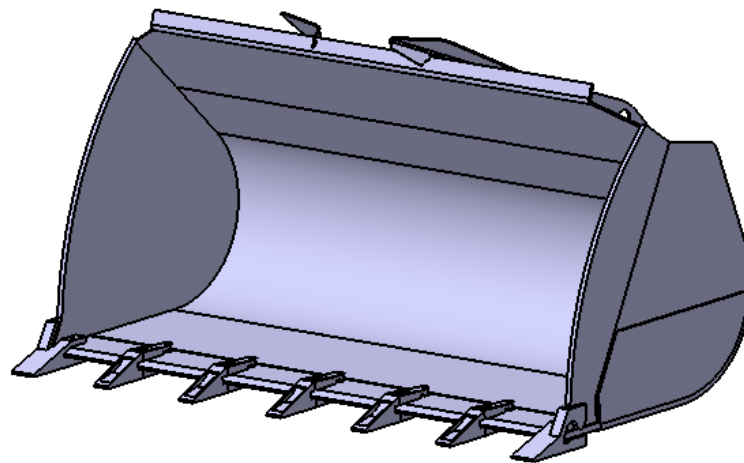


Figure 12. The bucket with chamfered teeth.

The length of each component on the working unit, as related to Equations (7) and (8), is measured when the bucket is in a level state, as Figure 13 presents. These lengths are detailed in Table 14.

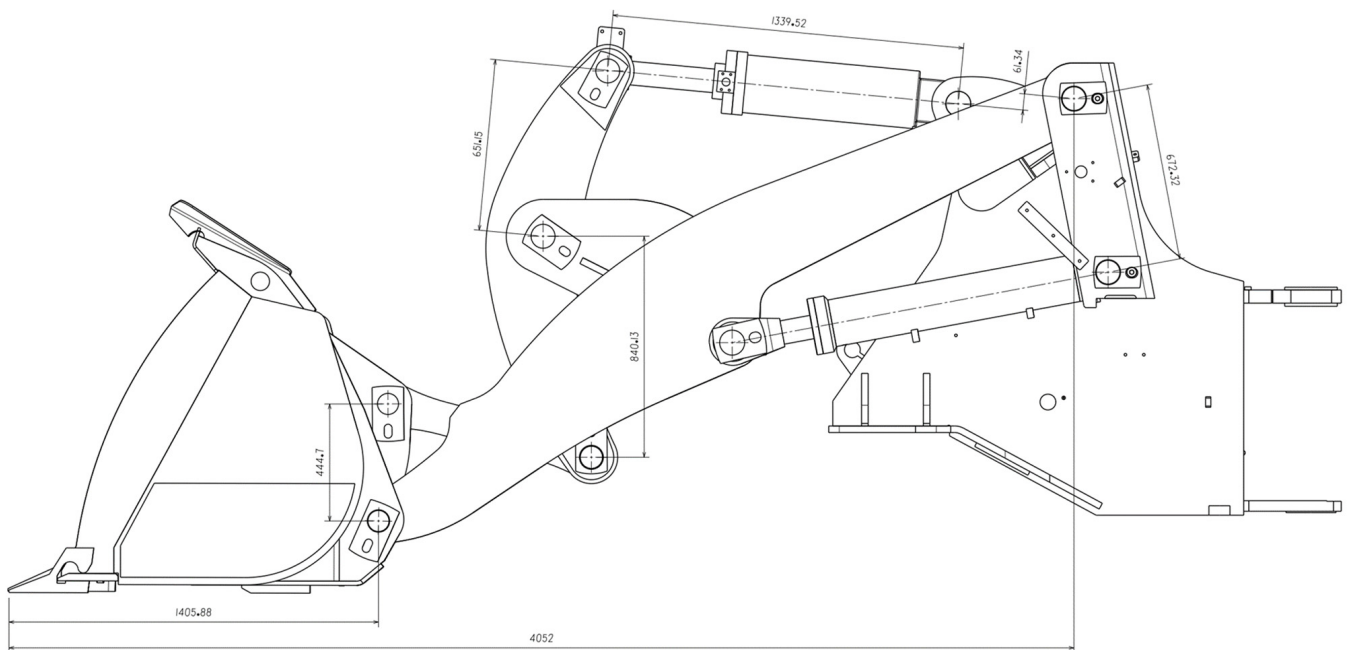


Figure 13. Dimensions of working unit when bucket is in level position.

Table 14. Dimensions of key components.

Items	L1	L2	L3	L4	L5	L6	L7
Length (mm)	4052	445	840	651	61	672	1406

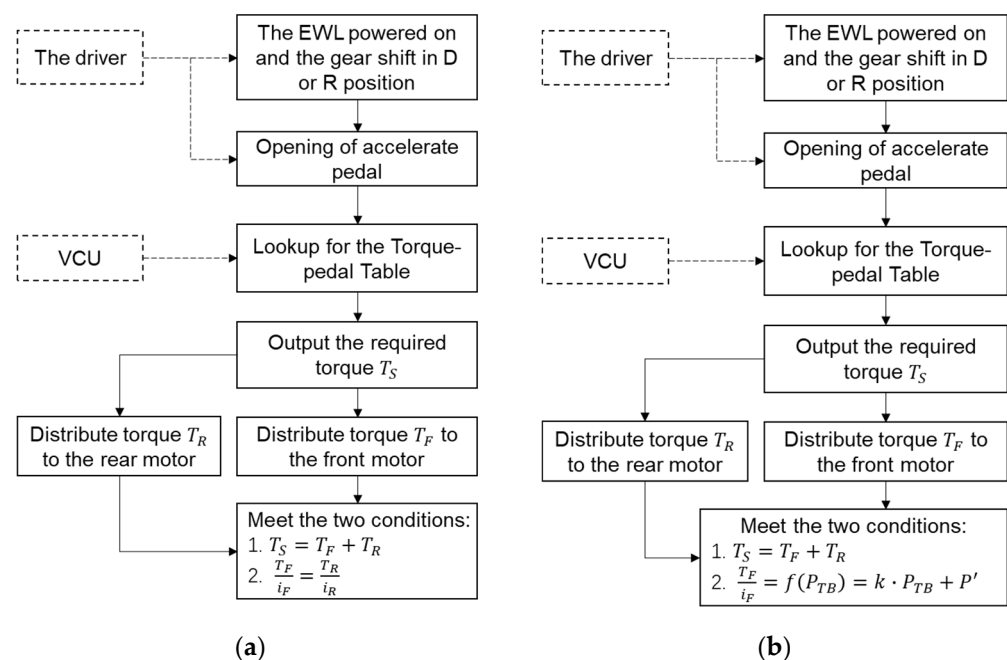
The parameters of the working motor are presented in Table 15.

Table 15. Parameters of working motor.

Items	Parameters	Items	Parameters
Motor type	PMSM	Model	UM100H31
Rated torque	400 N·m	Peak torque	1000 N·m
Rated power	75 KW	Peak power	155 KW
Rated speed	1910 rpm	Insulation level	H
Max. speed	4500 rpm	Protection level	IP67
Rated voltage	540 VDC	Cooling mode	Liquid
Mass	120 Kg	Max. efficiency	96%

3.5. The Control Methods on Torque Distribution

For the newly designed EWL, two control strategies for torque distribution have been implemented to assess their effectiveness in shoveling operations. The first strategy involves distributing an equal drive force to both the front and rear wheels, as mandated by the VCU in response to the opening of the accelerator pedal. This control scheme is described in Figure 14a. The second strategy entails distributing the force according to the wheel load, with the front load aligned with the hydraulic pressure in the base chamber of the tilt cylinder. Regardless of the method employed, the sum of the torque generated by the front and rear motors corresponds to the required torque based on the opening of the accelerator pedal. This second method is depicted in Figure 14b.

**Figure 14.** (a) Torque distributed evenly, and (b) torque distributed by wheel load.

4. Drive Effect of New Control Method

Using the newly developed EWL, a series of experiments on the drive force, front wheel slide, and rear wheel slide are carried out in the running condition and shoveling condition.

In the shoveling condition, the rear motor target speed is set to 600 rpm and the EWL is driven to move forward and backward three times.

In the shoveling condition, the EWL is operated to shovel sandstone in two torque distribution modes. The first strategy involves determining the driving torque by analyzing the accelerator pedal opening and subsequently allocating this torque evenly between the front and rear wheels. In the second strategy, the identified torque is distributed in proportion to the load on the front and rear wheels, while the load is calculated based on the pressure of the base chamber of the tilt cylinder.

4.1. Drive Force

4.1.1. Running Condition Force

The torque and speed curves of the drive motors in the running condition are shown in Figures 15–17. The drive forces on the wheels are calculated according to the motor torque, transmission ratio, and wheel radius. Specifically, in the dual-motor drive condition, the drive force is the sum of the front wheel drive force and rear wheel drive force.

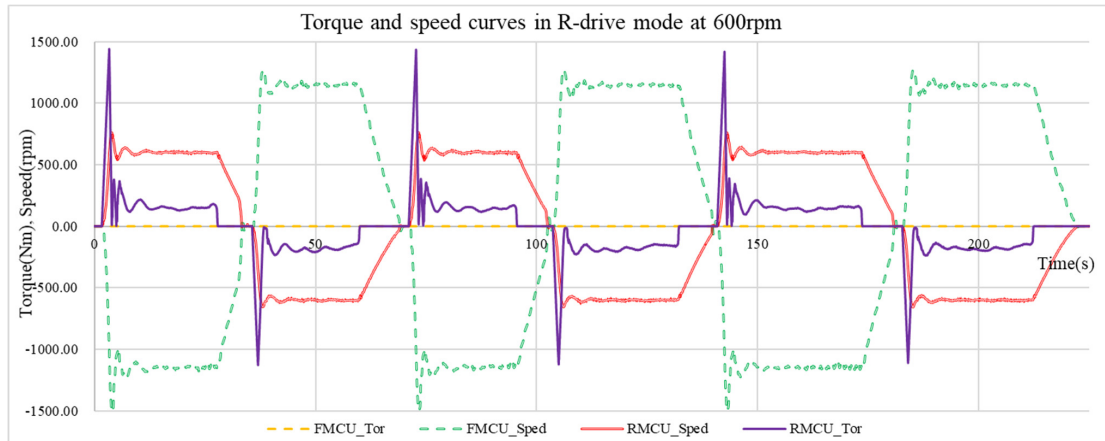


Figure 15. Torque and speed curves of motor in R–drive mode.

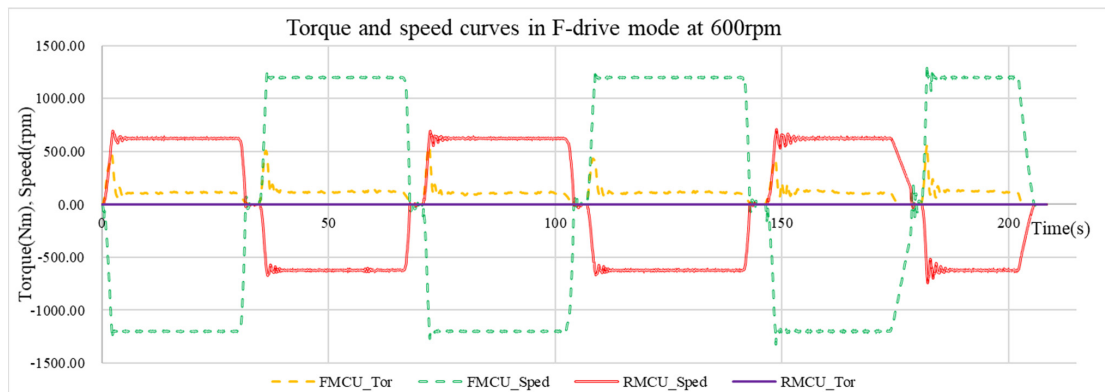


Figure 16. Torque and speed curves of motor in F–drive mode.

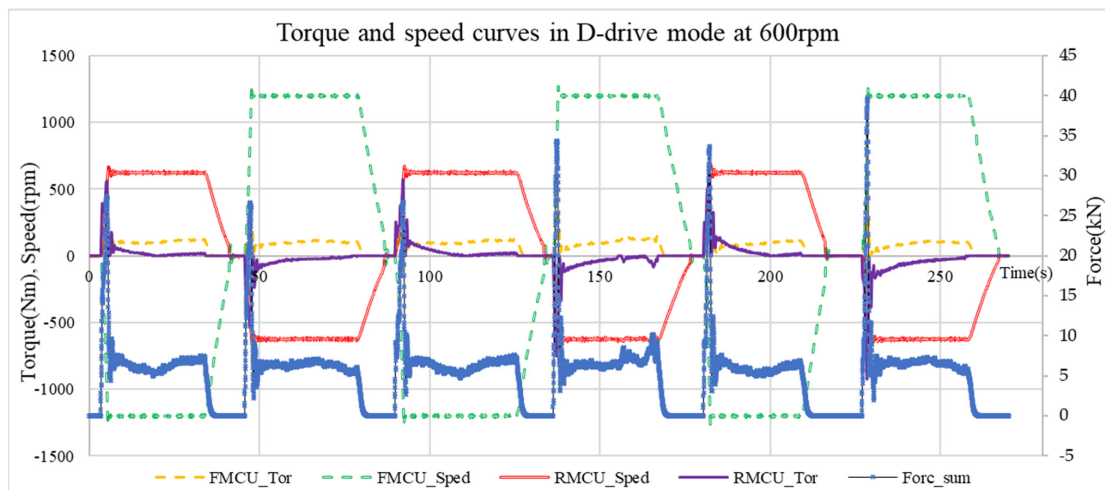


Figure 17. Torque and speed curves of motor in D–drive mode.

Figure 15 illustrates the torque and speed curves of the motor in rear drive mode, with the drive speed of the rear motor constrained to 600 rpm.

The data extracted from the stable periods of each operational state in Figure 15 have been computed and documented in Table 16. It indicates that the average torque of the rear motor varies between 149 N·m and 157.71 N·m during forward movement, whereas it fluctuates between 177.34 N·m and 178.68 N·m in reverse states. Regarding drive forces, the highest and lowest values are 4.16 kN and 4.48 kN, respectively, during forward movement. In reverse states, the maximum and minimum values are 5.07 kN and 5.04 kN, respectively.

Table 16. Data calculated in R-drive mode in running condition.

EWL State	Data Segment	\bar{T}_{R_Mot} (N·m)	\bar{F}_R (kN)
Forward 1	298–1311	157.71	4.48
Forward 2	3909–4711	146.63	4.16
Forward 3	7481–8623	149.00	4.23
Backward 1	2063–3002	178.74	5.07
Backward 2	5439–6581	177.34	5.03
Backward 3	9410–10,542	177.68	5.04

Figure 16 shows three phases of moving forward and backward in running condition in rear motor drive mode.

Figure 17 depicts the curves of the torque, speed, and drive force of the EWL in dual-motor drive mode, which is a combination of two drive motors and transmission systems. In this configuration, the drive force is theoretically the sum of the forces generated by the front and rear wheels.

As computed and detailed in Table 17, the data for the front motor drive reveal that the largest average torque during forward motion is 110.83 Nm, with the smallest being 106.13 Nm. Additionally, the maximum average torque peaks at 118.77 Nm, while the minimum value is 112.49 Nm. In terms of the average drive force, the highest and lowest values are recorded at 6.06 kN and 5.80 kN, respectively, during forward motion. In reverse states, the maximum and minimum values are 6.50 kN and 6.15 kN, respectively.

Table 17. Data calculated in F-drive mode in running condition.

EWL State	Data Segment	\bar{T}_{F_Mot} (N·m)	\bar{F}_F (kN)
Forward 1	148–1451	110.83	6.06
Forward 2	3707–5034	106.13	5.80
Forward 3	7526–8638	110.48	6.04
Backward 1	1894–3263	118.77	6.50
Backward 2	5589–7040	112.49	6.15
Backward 3	9235–10,046	117.24	6.41

Table 18 compiles the essential data derived from the calculations based on Figure 17. In Table 18, \bar{F}_R represents the average drive force on the rear wheels, \bar{F}_F denotes the average drive force on the front wheels, and \bar{F}_{Sum} signifies the sum of \bar{F}_R and \bar{F}_F .

Table 18. Data calculated in D-drive mode in running condition.

EWL State	Data Segment	\bar{T}_{R_Mot} (N·m)	\bar{T}_{F_Mot} (N·m)	\bar{F}_R (kN)	\bar{F}_F (kN)	\bar{F}_{Sum} (kN)
Forward 1	377–1584	17.66	106.39	0.50	5.82	6.32
Forward 2	4778–6191	22.92	102.79	0.65	5.62	6.27
Forward 3	9238–10,392	33.16	91.31	0.94	4.99	5.94
Backward 1	2521–3877	27.95	102.21	0.79	5.59	6.38
Backward 2	7032–8293	35.42	104.98	1.01	5.74	6.75
Backward 3	11,812–12,751	41.90	99.04	1.19	5.42	6.61

In forward movement, the peak value of the overall driving force \bar{F}_{Sum} is 6.32 kN, and the minimum value is 5.94 kN. During backward movement, the maximum of \bar{F}_{Sum} reaches 6.75 kN, and the minimum value descends to 6.38 kN.

In this set of tests, the drive force of the R-drive mode is the smallest among the three drive modes. Across each mode, backward movement consistently requires more drive force than forward movement. Specifically, in R-drive mode, the drive force for backward motion is generally 17.7% higher than that for forward motion. Similarly, in F-drive mode, the drive force for backward motion is 6.36% higher than for forward motion, and in D-drive mode, it is 6.63% higher than for forward motion. Importantly, it is noteworthy that the drive torque of the front motor is considerably lower than that of the rear motor in single motor drive modes. This underscores that a smaller motor on the front drive axle is sufficient to generate the required drive force for the EWL.

4.1.2. Shoveling Condition Force

1. Drive torque distributed evenly

The torque, speed, and drive force curves for three shoveling processes employing the evenly distributed torque strategy are illustrated in Figures 18–23, where F_F represents the current force on the front wheels, F_R is the force on the rear wheels, and Forc_sum means the sum of F_F and F_R.

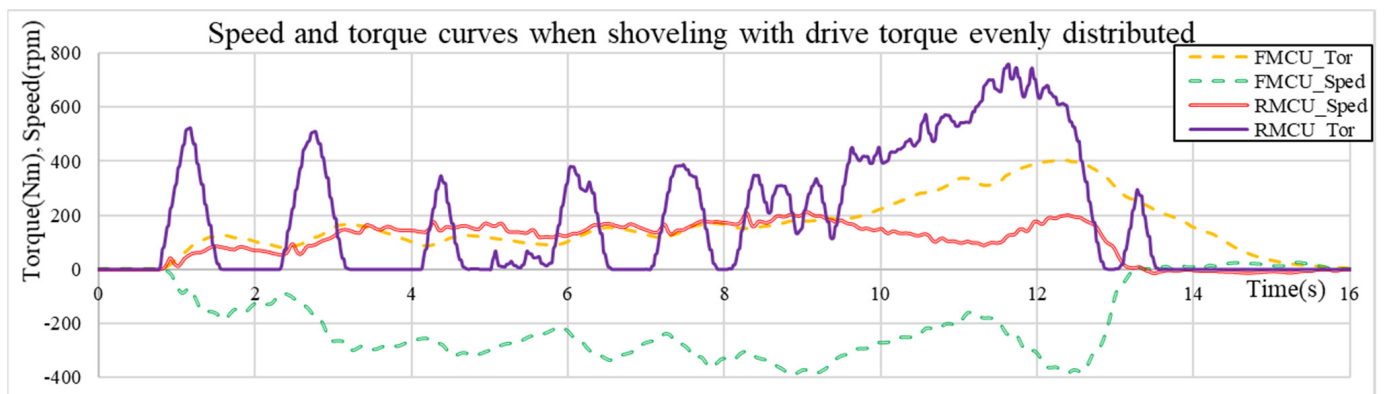


Figure 18. Speed and torque curves when shoveling with drive torque evenly distributed (first time).

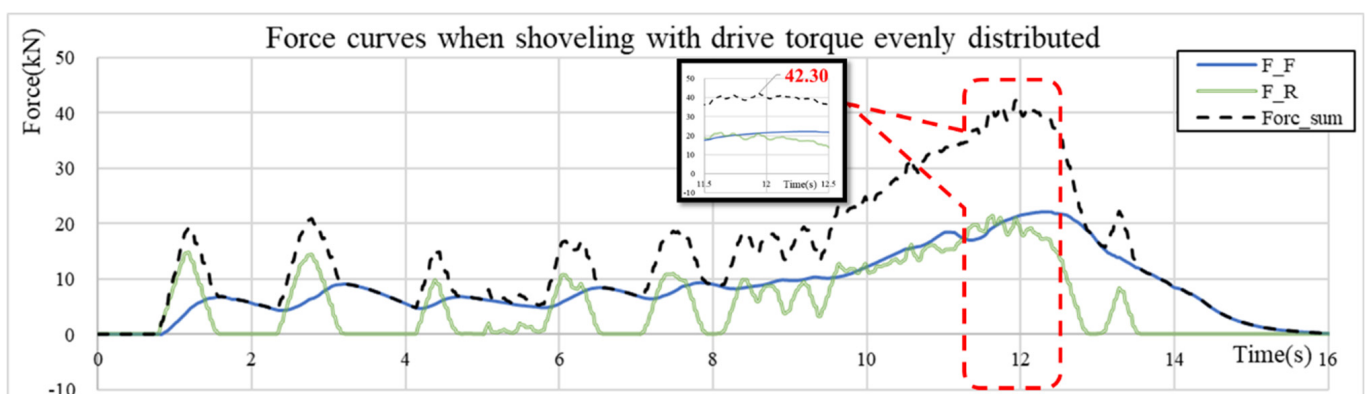


Figure 19. Force curves when shoveling with drive torque evenly distributed (first time).

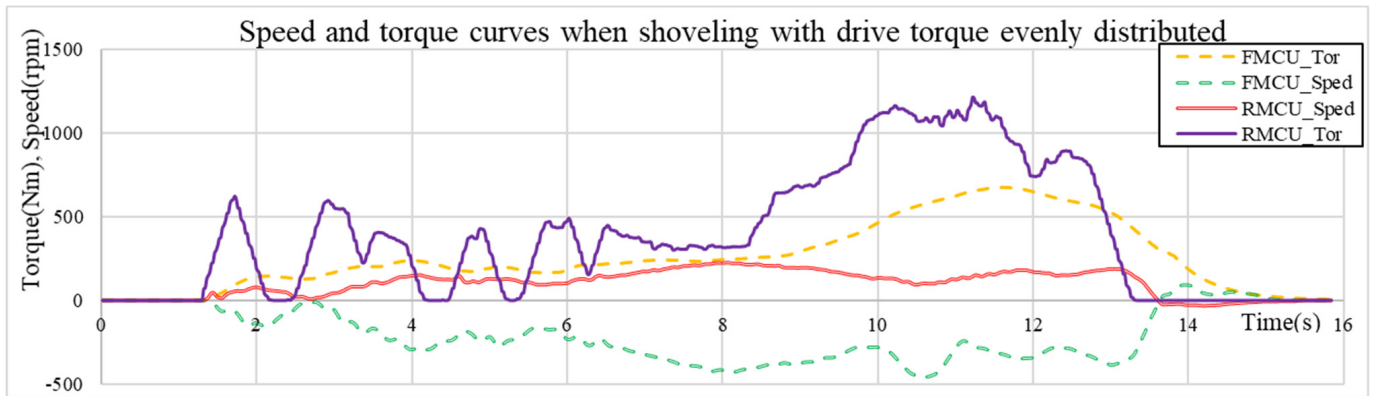


Figure 20. Speed and torque curves when shoveling with drive torque evenly distributed (second time).

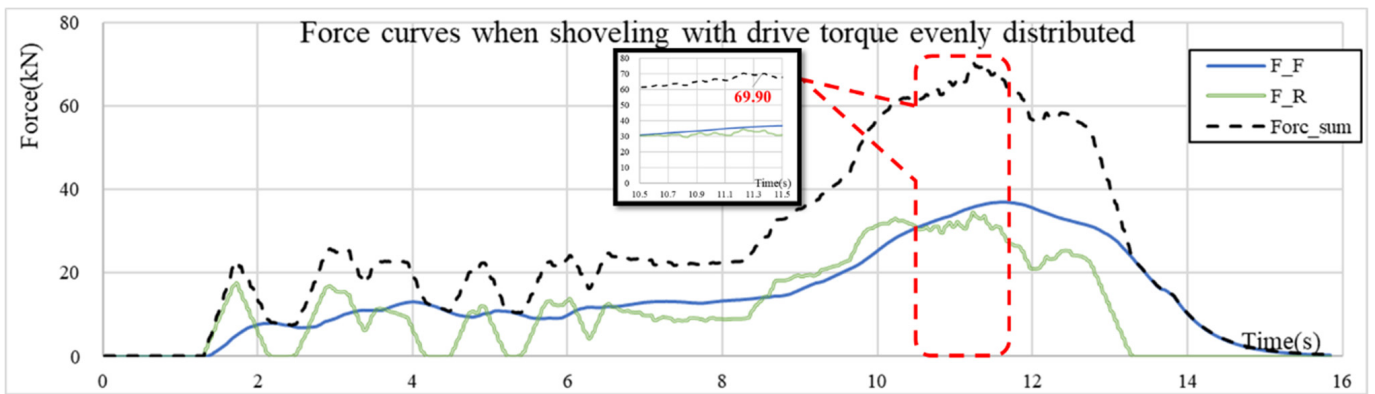


Figure 21. Force curves when shoveling with drive torque evenly distributed (second time).

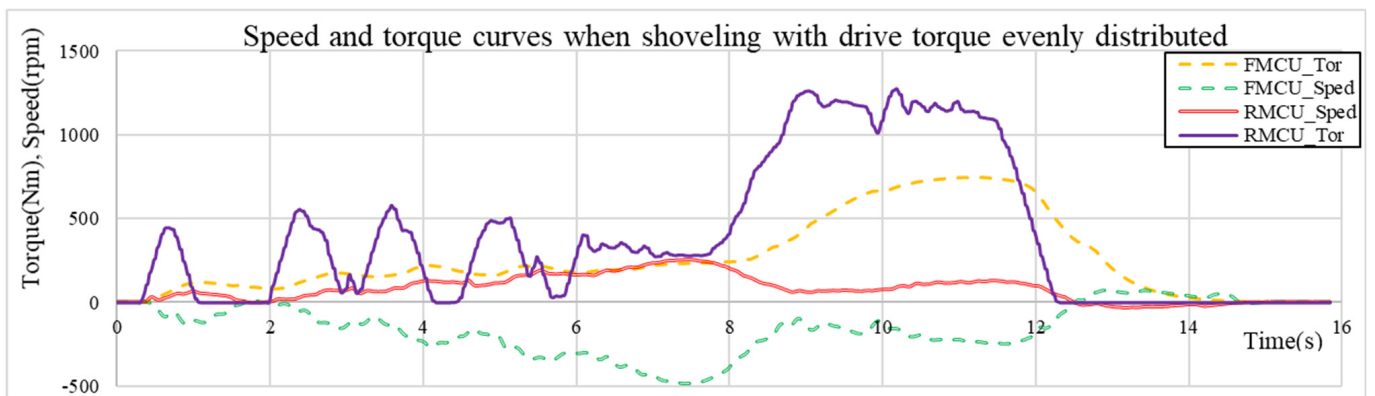


Figure 22. Speed and torque curves when shoveling with drive torque evenly distributed (third time).

Figures 18–22 are torque and speed curves, revealing a smooth variation in the speed of both the front and rear motors. However, notable differences are observed in the torque profiles, with the rear motor exhibiting larger fluctuations compared to the front motor.

In Figure 18, around the 9.4 s mark, the EWL initiates the shoveling process on the material pile, leading to a corresponding increase in the force applied to the bucket. Subsequently, at 11.94 s, the overall drive force attains its maximum value, reaching 42.3 kN, as indicated in Figure 19.

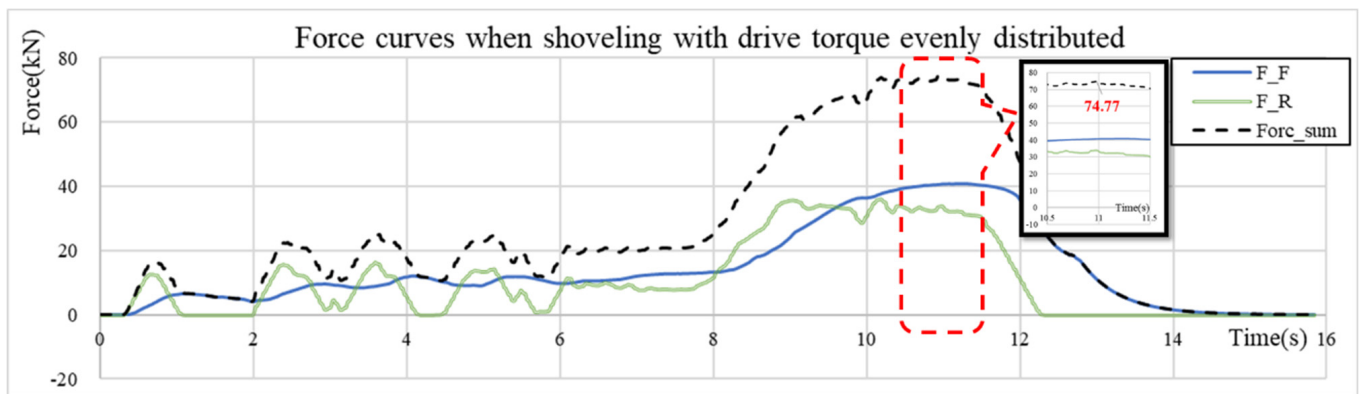


Figure 23. Force curves when shoveling with drive torque evenly distributed (third time).

In Figure 20, around the 8.3 s mark, the EWL starts the shoveling process on the material pile. Subsequently, at 11.36 s, the overall drive force reaches its maximum value of 69.9 kN, as indicated in Figure 21. The second shoveling process lasts about 4 s.

In Figure 22, the shoveling motion on the material pile begins at around 7.7 s. Later, at 10.98 s, the overall drive force increases to its peak value of 74.77 kN, as marked in Figure 23. This shoveling process ends at about 12.3 s.

It appears that the forces on the front wheels remain relatively stable compared to those on the rear wheels. Notably, during the bucket's shoveling of the material pile, F_F surpasses F_R and maintains this trend until the end of the shoveling process. This set of shoveling tests further illustrates that the design of the new EWL, featuring a smaller motor and a higher transmission ratio, is capable of generating sufficient drive forces for effective material shoveling.

2. Drive torque distributed by wheel load

A series of tests were conducted under shoveling conditions, incorporating the torque distribution method outlined in Section 2.3. The drive force distribution adheres to the wheel load, signifying that higher loads on the front wheels result in the generation of more torque on the front motor. This principle similarly applies to the rear motor, where increased rear wheel loads correspond to higher torque generation on the rear motor. Figures 24 and 25 are the torque, speed, and force curves of the shoveling processes.

Figure 24 shows that the front motor that generates torque still has more smooth fluctuation than the rear motor. The peak torque of the two motors occurred at different times during the same shoveling process. Specifically, in the third shoveling process, the EWL climbed the material and subsequently skidded back, which can be reflected by the change in speed direction around the 14.3 s mark.

In Figure 25, it is noticeable that the force on the front wheels consistently exceeds that on the rear wheels for the majority of the time. During shoveling phases II and III, which commence at approximately 8 s and conclude around 16 s, the bucket initiates the shoveling of substantial material. In these periods, it becomes evident that the front and rear forces are relatively close in the initial stages. However, as the shoveling progresses, the front force significantly increases in the later part. This observation suggests that the mass on the bucket shifts the gravity center of the EWL towards the front, resulting in an increase in front wheel load. Consequently, the force on the front wheels becomes notably larger than that on the rear wheels, as indicated by the curves.

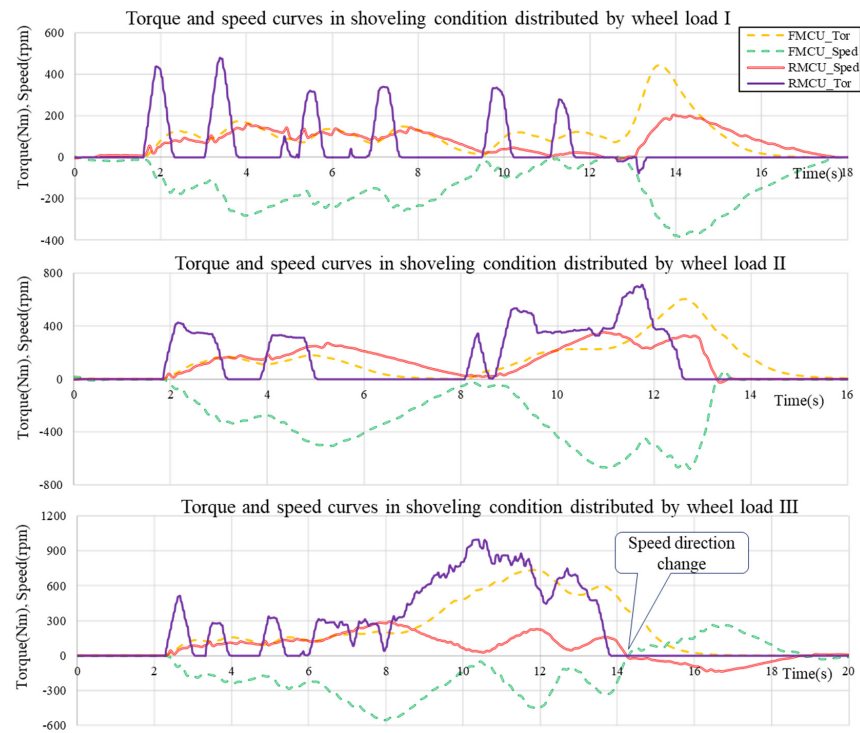


Figure 24. Torque and speed curves when shoveling with drive torque distributed by wheel load.

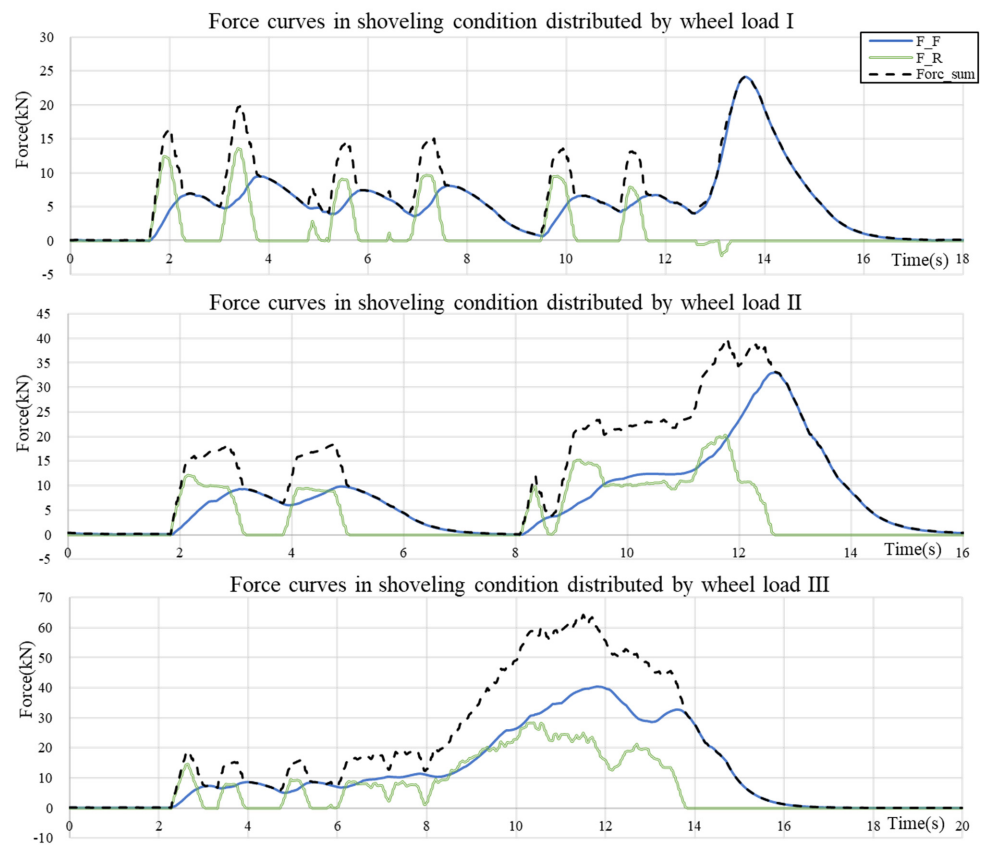


Figure 25. Force curves when shoveling with drive torque distributed by wheel load.

4.2. Tire Slip

Based on Figures 18, 20, 22, and 24, the motor speed is multiplied by the corresponding gear ratio without accounting for the mechanical efficiency and the differential speed

between the coaxial wheels. This calculation is performed to generate a wheel speed curve, facilitating the comparison of tire slippage.

The calculated wheel speed curves of the two shoveling conditions are drawn in Figure 26 and Figure 27, respectively.

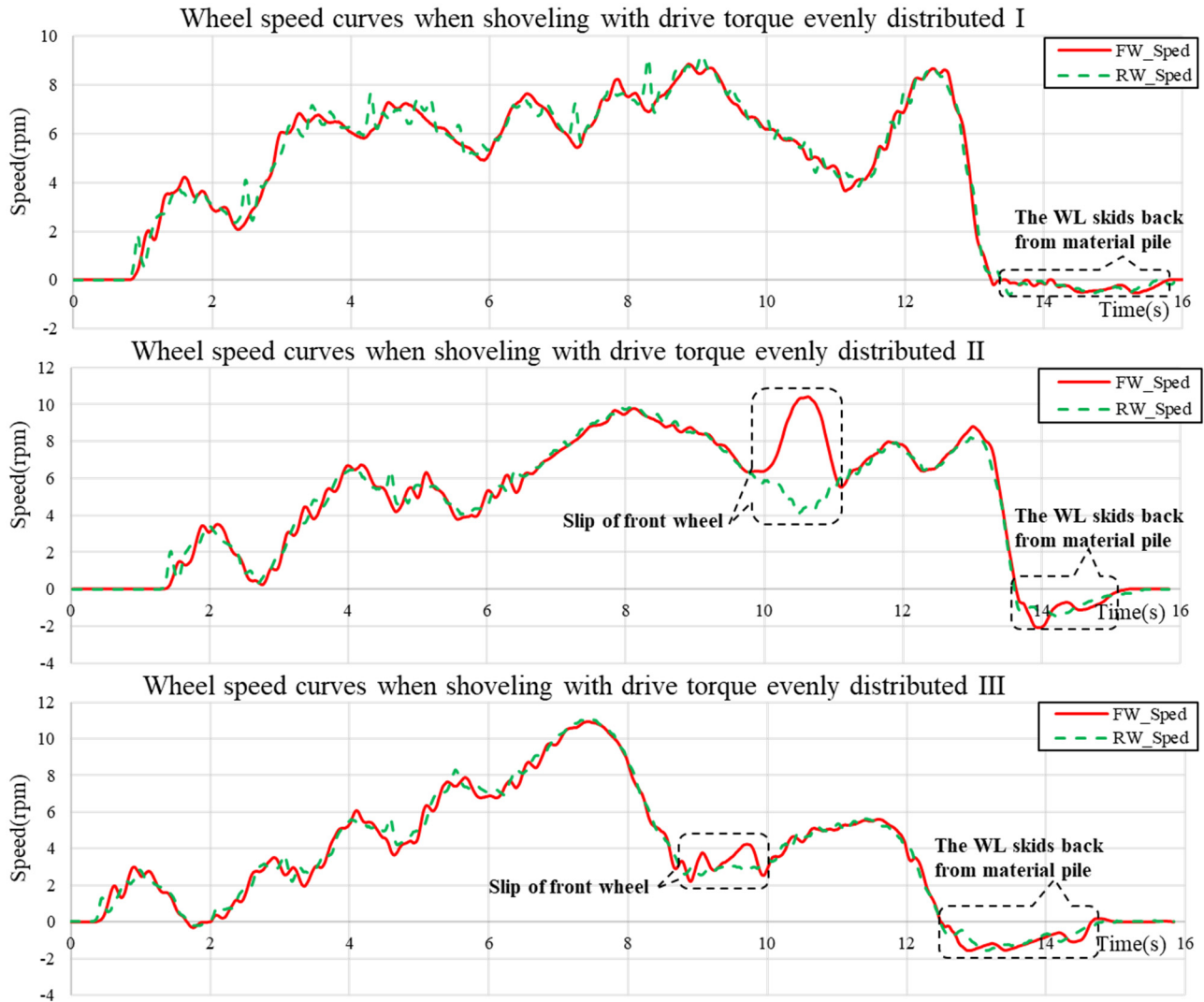


Figure 26. Wheel speed curves when shoveling with drive torque is evenly distributed.

In the cases of drive torque being evenly distributed, as observed in the curves presented in Figure 26, there is minimal wheel sliding in the first case when the bucket is shoveling the material pile. In the second case, the front wheel rotates at a higher speed than the rear one starting from the 9.8 s mark, and this difference becomes more pronounced until the 11 s mark when the two speeds become closer. This indicates the occurrence of front wheel slippage during this time range. In the third case, slippage is observed from the 8.8 s mark to the 10.1 s mark, but the difference in wheel speeds is smaller than that in the second case.



Figure 27. Wheel speed curves when shoveling with drive torque is distributed by wheel load.

In each of these three cases, the EWL experiences skidding back at the conclusion of the shoveling process, and these instances are specifically marked in the curve graphics.

In the cases where the drive torque is distributed by the wheel load, as depicted in the curves shown in Figure 27, there is no evident wheel slippage during the shoveling processes, both in the preparation stages and when shoveling material piles. A minor slip occurs at the beginning of shoveling the material pile in the first case and occurs at the end of shoveling the material pile in the second case, with the slip duration being very short.

Upon comparing Figures 26 and 27, it becomes evident that the shoveling process exhibits significantly less wheel slippage when the drive torque of the front and rear wheels is distributed according to the wheel load. This observation is expected to contribute to the reduction in or elimination of parasitic power.

5. Discussions and Conclusions

5.1. The Relationship between the Hydraulic Pressure and Vertical Axle Load

The results of the hydraulic pressure of the working unit of the EWL yielded noteworthy findings. A pronounced correlation was identified between the vertical force applied to the front wheel of the EWL and the hydraulic pressure within the base chamber of the tilt cylinder.

On one hand, it is important to emphasize the theoretical derivation of this correlation, which has been thoroughly analyzed. Equation (7) describes the relationship between N_{f4} and N_{f1} , while Equation (8) illustrates the relationship between N_{f4} and N_{f3} . Therefore, the relationship between N_{f3} and N_{f1} can be derived and is presented in Equation (15).

$$N_{f3} = \frac{L_3 \cdot L_7}{L_2 \cdot L_4} \cdot N_{f1} \quad (15)$$

This indicates a linear relationship between N_{f3} and N_{f1} , where N_{f1} is the summed forces acting on the bucket in the vertical direction, and N_{f3} reflects a linear relationship to the hydraulic pressure of the base chamber of the tilt cylinder. Meanwhile, for a WL, the vertical force on the bucket and the vertical force applied to the front wheel have a relationship as shown in Figure 28, where F_{Bct_y} is similar to N_{f1} , L_{Br} represents the horizontal distance from the tip of the bucket to the front axle, a denotes the horizontal distance from the front axle to the center of mass, and b signifies the horizontal distance from the center of mass to the rear axle. The symbol G represents the total mass of the wheel loader. Additionally, N_F and N_R denote the vertical forces on the front and rear wheels, respectively, which correspond to the vertical axle loads on the front and rear axles.

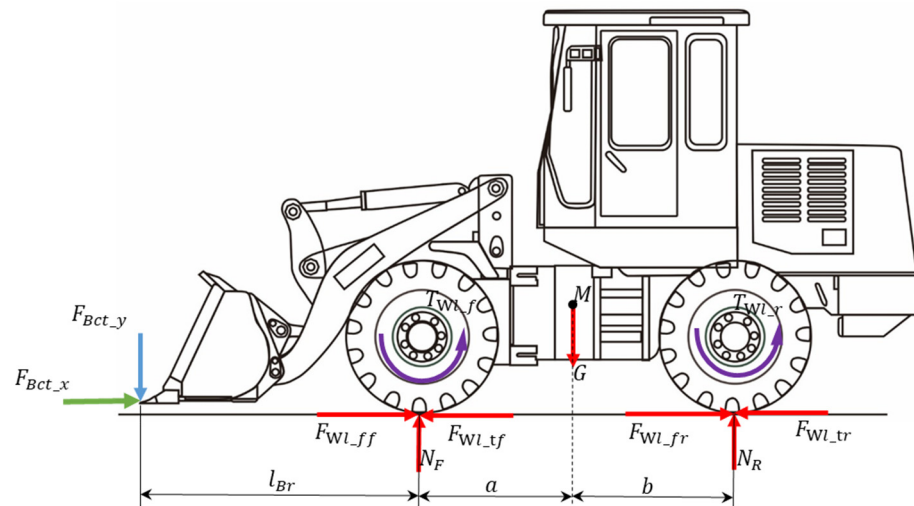


Figure 28. The forces on an EWL of a simplified case.

To achieve force equilibrium, the relationship between these forces adheres to Equation (16), from which Equation (17) is derived. Equation (17) demonstrates a linear relationship between the front axle load and the vertical force on the bucket, for the other parameters can be measured.

$$F_{Bct_y} \cdot (l_{Br} + a + b) + G \cdot b = N_F \cdot (a + b) \quad (16)$$

$$N_F = \frac{L_{Br} + a + b}{a + b} \cdot F_{Bct_y} + \frac{b}{a + b} \cdot G \quad (17)$$

Therefore, the relationship between the pressure on the base chamber of the tilt cylinder and the front axle load is linear.

On the other hand, weighing tests conducted on a 15 ton EWL have also demonstrated a nearly linear relationship between the pressure on the base chamber of the tilt cylinder and the front axle load, as illustrated in Figure 5. Notably, this correlation demonstrates an approximate linearity, imparting valuable insights crucial for the design and control considerations of novel EWLs. These findings serve as pivotal reference points, offering guidance to enhance the performance and efficiency of evolving EWLs. However, it is uncertain whether the method is applicable to super heavy EWLs such as a 35 ton EWLs.

5.2. The Design and Testing of the New EWL

Through the implementation of tests under both running and shoveling conditions with the newly designed EWL, the results confirm that a substantial transmission ratio facilitates the use of a motor with lower rated torque on the front drive axle while still providing sufficient force for the WL.

In the traditional design of EWLs, two identical drivetrains, each comprising the same drive motors in the front and rear axles, are commonly employed. However, this design suffers from two main drawbacks. Firstly, it fails to fully utilize the drive torque and power capabilities of both the front and rear motors. Secondly, it results in increased production costs for the WLs.

In the new design introduced in this research, a PMSM and a SRM are respectively installed in the rear and front axles of the EWL. The transmission ratio of the front drivetrain is set at 44.03, while the rear transmission ratio is 22.85. This configuration ensures that if the EWL is driven by a single motor, the front motor is capable of generating sufficient drive force on the wheels. Additionally, if the drive force proves to be inadequate, the rear motor can be engaged simultaneously with the front motor.

The primary advantage of this design is evident when the EWL is engaged in material shoveling operations. In this scenario, the front wheels are capable of generating nearly double the drive force compared to the old design. This enhancement is particularly beneficial during the shoveling process, as it helps to counteract the forward shift of the center of gravity, which often results in the lifting of the rear wheels. This lifting reduces the adhesion force between the rear wheels and the ground, thereby potentially limiting the ability of the rear motor to generate sufficient torque if the rear wheels do not slip.

Due to cost constraints, the utilization of multiple types of motors with varying rated torque and power has not been explored in this research. However, this area warrants further investigation.

Lastly, a comparison between two control methods, namely evenly distributed drive torque and distribution based on wheel load, has been conducted. The disadvantage of evenly distributing drive torque is that the rear wheels may slip if the rear drive force exceeds the adhesion force, while the front wheels may lack the necessary drive force to propel the EWL forward. In contrast, distributing torque according to the wheel load, which is correlated with the hydraulic pressure of the base chamber of the tilt cylinder and can be measured using a hydraulic pressure sensor, proves to be a more feasible approach. The testing results indicate that the latter method significantly reduces tire slippage during shoveling operations, thereby demonstrating a more effective control strategy.

Author Contributions: Methodology, X.F., Y.H. and M.A.A.; software, X.F., Y.H. and W.S.; formal analysis, X.F.; writing—original draft, X.F. and M.A.A.; writing—review and editing, S.V.W.; visualization, M.A.A.; supervision, Y.H. and S.V.W.; project administration, Y.H. and S.V.W.; funding acquisition, X.F. and W.S. All authors have read and agreed to the published version of the manuscript.

Funding: This research was funded by the Sudian Yingcai Engineering Project from the Jiangsu Vocational College of Electronics and Information, the Huai'an City Science and Technology project grant number [HABL202127], the Huai'an City Science and Technology guidance project grant number [HABZ202319], and Huai'an New Energy Vehicle Technology Public Service Platform grant number [HAP202313]. The APC was funded by [HABZ202319] and [HAP202313].

Data Availability Statement: The data presented in this study are available on request from the corresponding author. The data are not publicly available as the data belongs to the core information for enterprise product research and market competition.

Acknowledgments: We extend our heartfelt appreciation to the Jiangsu Province Vocational College Teachers' Study Visit and Training Program 2024 as well as the Jiangsu Intelligent Unmanned Equipment Industry Innovation Center for their generous support in providing facilities and accommodation.

Conflicts of Interest: On behalf of all the authors, the corresponding author states that there are no conflicts of interest.

Abbreviations

CAMA	China Construction Machinery Association
EWL	Electric wheel loader
PMSM	Permanent Magnet Synchronous Motor
SRM	Switched reluctance motor
WL	Wheel loader

References

1. Tan, X.; Li, H.; Guo, J.; Gu, B.; Zeng, Y. Energy-saving and emission-reduction technology selection and CO₂ emission reduction potential of China's iron and steel industry under energy substitution policy. *J. Clean. Prod.* **2019**, *222*, 823–834. [CrossRef]
2. Joshi, A. Review of vehicle engine efficiency and emissions. *SAE Int. J. Adv. Curr. Pract. Mobil.* **2020**, *2*, 2479–2507. [CrossRef]
3. Cai, W.; Wu, X.; Zhou, M.; Liang, Y.; Wang, Y. Review and development of electric motor systems and electric powertrains for new energy vehicles. *Automot. Innov.* **2021**, *4*, 3–22. [CrossRef]
4. Qiao, Q.; Zhao, F.; Liu, Z.; He, X.; Hao, H. Life cycle greenhouse gas emissions of Electric Vehicles in China: Combining the vehicle cycle and fuel cycle. *Energy* **2019**, *177*, 222–233. [CrossRef]
5. Li, X.; Duan, C.; Bai, K.; Yao, Z. Operating Performance of Pure Electric Loaders with Different Types of Motors Based on Simulation Analysis. *Energies* **2021**, *14*, 617. [CrossRef]
6. CCMA. Available online: <http://www.cncma.org/article/19096> (accessed on 29 January 2024).
7. Yang, Z.; Wang, J.; Han, Y. A novel real-time center of gravity estimation method for wheel loaders with front/rear-axle-independent electric driving. *J. Control. Sci. Eng.* **2021**, *2021*, 6621060. [CrossRef]
8. Zhang, H.; Wang, F.; Xu, B.; Fiebig, W. Extending battery lifetime for electric wheel loaders with electric-hydraulic hybrid powertrain. *Energy* **2022**, *261*, 125190. [CrossRef]
9. Wei, J.; Zhao, J.; Wang, J. Research on Shovel-Force Prediction and Power-Matching Optimization of a Large-Tonnage Electric Wheel Loader. *Appl. Sci.* **2023**, *13*, 13324. [CrossRef]
10. Wang, F.; Zhang, Q.; Wen, Q.; Xu, B. Improving productivity of a battery powered electric wheel loader with electric-hydraulic hybrid drive solution. *J. Clean. Prod.* **2024**, *440*, 140776. [CrossRef]
11. Yu, S.; Zhao, G.; Song, X.; Sun, Z. Control oriented model order reduction for the hydraulic system of an autonomous wheel loader. *Control Eng. Pract.* **2023**, *139*, 105628. [CrossRef]
12. Fei, X.; Han, Y.; Wong, S.V. An Overview of and Prospects for Research on Energy Savings in Wheel Loaders. *Automot. Exp.* **2023**, *6*, 133–148. [CrossRef]
13. Yuan, X.; Wang, J. Torque distribution strategy for a front-and rear-wheel-driven electric vehicle. *IEEE Trans. Veh. Technol.* **2012**, *61*, 3365–3374. [CrossRef]
14. Kwon, K.; Seo, M.; Min, S. Efficient multi-objective optimization of gear ratios and motor torque distribution for electric vehicles with two-motor and two-speed powertrain system. *Appl. Energy* **2020**, *259*, 114190. [CrossRef]
15. Li, B.; Goodarzi, A.; Khajepour, A.; Chen, S.-K.; Litkouhi, B. An optimal torque distribution control strategy for four-independent wheel drive electric vehicles. *Veh. Syst. Dyn.* **2015**, *53*, 1172–1189. [CrossRef]
16. Lin, C.; Liang, S.; Chen, J.; Gao, X. A multi-objective optimal torque distribution strategy for four in-wheel-motor drive electric vehicles. *IEEE Access* **2019**, *7*, 64627–64640. [CrossRef]
17. Dizqah, A.M.; Lenzo, B.; Sornioti, A.; Gruber, P.; Fallah, S.; De Smet, J. A fast and parametric torque distribution strategy for four-wheel-drive energy-efficient electric vehicles. *IEEE Trans. Ind. Electron.* **2016**, *63*, 4367–4376. [CrossRef]
18. Yang, Z.; Wang, J.; Gao, G.; Shi, X. Research on Optimized Torque-Distribution Control Method for Front/Rear Axle Electric Wheel Loader. *Math. Probl. Eng.* **2017**, *2017*, 7076583. [CrossRef]
19. Gao, G.; Wang, J.; Ma, T.; Han, Y.; Yang, X.; Li, X. Optimisation strategy of torque distribution for the distributed drive electric wheel loader based on the estimated shovelling load. *Veh. Syst. Dyn.* **2022**, *60*, 2036–2054. [CrossRef]
20. Wang, Y.Y.; Hu, Y.; Ming, Q. Torque Distribution Control Strategy of Electric Wheel Loader with Multiple Drive Motors Based on Optimal Motor Efficiency. *SAE Int. J. Commer. Veh.* **2023**, *16*, 257–269. [CrossRef]
21. Fei, X.; Shenrui, H.; Voon, W.S.; Azman, M.A.; Yunwu, H. Mechanical Characteristics of Distributed Electric Wheel Loader in Shoveling Condition. *Automot. Exp.* **2023**, *6*, 336–358. [CrossRef]
22. Fei, X.; Han, Y.; Wong, S.V.; Azman, M.A. Efficiency Comparison of Electric Wheel Loader Powertrains with Dual Motor Input in Distributed Driving Modes. *World Electr. Veh. J.* **2023**, *14*, 298. [CrossRef]
23. He, B.; Zhang, C.; Cao, X.; Li, G.; Xiong, X. An approach to recognizing the working cycle stage with small sample data for energy conservation. *J. Clean. Prod.* **2023**, *414*, 137771. [CrossRef]
24. Bavendiek, I.R.; Kremmer, M.; Pfab, I.H. Selected Machine Examples. In *Mobile Working Machines*; SAE: Warrendale, PA, USA, 2020; p. 323.
25. Sidebotham, G. Open Systems: Pumps and Turbines. In *An Inductive Approach to Engineering Thermodynamics*; Springer: Berlin/Heidelberg, Germany, 2022; pp. 235–300.
26. Yueying, Z.; Chuantian, Y.; Yuan, Y.; Weiyang, W.; Chengwen, Z. Design and optimisation of an In-wheel switched reluctance motor for electric vehicles. *IET Intell. Transp. Syst.* **2019**, *13*, 175–182. [CrossRef]

27. Gaafar, M.A.; Abdelmaksoud, A.; Orabi, M.; Chen, H.; Dardeer, M. Switched reluctance motor converters for electric vehicles applications: Comparative review. *IEEE Trans. Transp. Electrification* **2022**, *9*, 3526–3544. [[CrossRef](#)]
28. Lin, T.; Lin, Y.; Ren, H.; Chen, H.; Chen, Q.; Li, Z. Development and key technologies of pure electric construction machinery. *Renew. Sustain. Energy Rev.* **2020**, *132*, 110080. [[CrossRef](#)]
29. Fernandes, J.O.F.; Bhagubai, P.P.; Branco, P.J. Recent Developments in Electrical Machine Design for the Electrification of Industrial and Transportation Systems. *Energies* **2022**, *15*, 6390. [[CrossRef](#)]

Disclaimer/Publisher’s Note: The statements, opinions and data contained in all publications are solely those of the individual author(s) and contributor(s) and not of MDPI and/or the editor(s). MDPI and/or the editor(s) disclaim responsibility for any injury to people or property resulting from any ideas, methods, instructions or products referred to in the content.